Astronomy
&
Astrophysics

Simultaneous and panchromatic observations of the fast radio burst FRB 20180916B[*]

M. Trudu[1,2], M. Pilia[2], L. Nicastro[3], C. Guidorzi[4,3,5], M. Orlandini[3], L. Zampieri[6], V. R. Marthi[7], F. Ambrosino[8,9], A. Possenti[2,1], M. Burgay[2], C. Casentini[8,10], I. Mereminskiy[11], V. Savchenko[12], E. Palazzi[3], F. Panessa[8], A. Ridolfi[2], F. Verrecchia[13,14], M. Anedda[1], G. Bernardi[15,16,17], M. Bachetti[2], R. Burenin[11], A. Burtovoi[18], P. Casella[14], M. Fiori[19], F. Frontera[4], V. Gajjar[20], A. Gardini[21,22], M. Ge[23], A. Guijarro-Román[22], A. Ghedina[24], I. Hermelo[22], S. Jia[23], C. Li[23], J. Liao[23], X. Li[23], F. Lu[23], A. Lutovinov[11], G. Naletto[19,6], P. Ochner[19,6], A. Papitto[4], M. Perri[13,14], C. Pittori[13,14], B. Safonov[25], A. Semena[11], I. Strakhov[25], M. Tavani[8,26], A. Ursi[8], S. L. Xiong[23], S. N. Zhang[23,27], and S. Zheltoukhov[25]

(Affiliations can be found after the references)

ABSTRACT

Aims. Fast radio bursts are bright radio transients whose origins are not yet understood. The search for a multi-wavelength counterpart of those events can set a tight constraint on the emission mechanism and the progenitor source.

Methods. We conducted a multi-wavelength observational campaign on FRB 20180916B between October 2020 and August 2021 over eight activity cycles of the source. Observations were carried out in the radio band by the SRT both at 336 and 1547 MHz and the uGMRT at 400 MHz. Simultaneous observations were conducted by the optical telescopes Asiago (*Galileo* and *Copernico*), CMO SAI MSU, CAHA 2.2 m, RTT-150 and TNG, and X/γ-ray detectors on board the AGILE, *Insight*–HXMT, INTEGRAL, and *Swift* satellites.

Results. We present the detection of 14 new radio bursts detected with the SRT at 336 MHz and seven new bursts with the uGMRT from this source. We provide the deepest prompt upper limits in the optical band for FRB 20180916B to date. In fact, the TNG/SiFAP2 observation simultaneous to a burst detection by uGMRT gives an upper limit $E_{\rm optical}/E_{\rm radio} < 1.3 \times 10^2$. Another burst detected by the SRT at 336 MHz was also co-observed by *Insight*–HXMT. The non-detection in the X-rays yields an upper limit (1−30 keV band) of $E_{\rm X-ray}/E_{\rm radio}$ in the range of $(0.9−1.3) \times 10^7$, depending on the model that is considered for the X-ray emission.

Key words. methods: observational – instrumentation: photometers – X-rays: bursts – stars: magnetars – stars: neutron – stars: flare

1. Introduction

Fast radio bursts (FRBs, for a review see e.g., Petroff et al. 2022) are intense ($10^{36−40}$ erg) radio flashes of millisecond-duration that travel extragalactic distances. The origin of these astrophysical transients is still a matter of debate. Most of them appear to be sporadic single events and only a small percentage of them exhibit a repeating behaviour (see e.g., Spitler et al. 2016; CHIME/FRB Collaboration 2019b).

Discovered by the CHIME telescope as the third known repeater (CHIME/FRB Collaboration 2019a), FRB 20180916B (R3) is the first FRB for which periodic activity was detected (CHIME/FRB Collaboration 2020). It has a period of 16.33 ± 0.12 days (Pleunis et al. 2021; CHIME/FRB Collaboration 2020) with an active window of ±2.6 days as observed at CHIME's frequencies: 400–800 MHz. Soon afterwards, periodic activity was also claimed for the first discovered repeater, FRB 20121102A (R1, Spitler et al. 2016, 2014), with an activity period of about 160 days and a duty cycle of ~54% (Cruces et al. 2021; Rajwade et al. 2020).

The R3 detections at different radio frequencies, ranging from ~150 MHz (Pastor-Marazuela et al. 2021; Pleunis et al. 2021) to 6 GHz (Bethapudi et al. 2022), indicate a chromatic pattern in the burst occurrence. The bursts at higher and lower fre-

quencies than CHIME only partially overlap with the CHIME active phase window. Specifically, bursts detected at 1.4 GHz, such as those detected by Apertif (Pastor-Marazuela et al. 2021), have an occurrence distribution shifted ~0.7 days earlier (i.e. earlier activity phases) compared to the CHIME detected ones. In contrast, bursts detected at the lower LOFAR frequencies show a phase shift of ~3 days (i.e. later activity phases; Pleunis et al. 2021). The differences in the active window include not only the different onset times but also the duration: the higher frequency active phases seem to last shorter than the lower frequency ones (Bethapudi et al. 2022; Pastor-Marazuela et al. 2021). Meanwhile, the average width of the bursts becomes larger at lower frequencies (Pastor-Marazuela et al. 2021). Although scattering contributes to this effect, it is generally limited to only the lowest frequencies for this FRB (Marcote et al. 2020; Pilia et al. 2020; Pastor-Marazuela et al. 2021).

Although the origin of FRBs remains an open question, most of the current models consider highly magnetised neutron stars (i.e. magnetars) as one of the most plausible FRB progenitors (Margalit et al. 2020; Beloborodov 2017; Lyubarsky 2014). The magnetar models predict the FRB event to happen either via magnetic reconnection in the neutron star magnetosphere or via shock(s) due to the interaction of a powerful magnetar outflow with the surrounding medium (see e.g., Zhang 2022, for a comprehensive review). The FRB-magnetar link was strengthened with the detection of a radio burst similar to an FRB from the Galactic

---

magnetar SGR J1935+2154 (CHIME/FRB Collaboration 2020; Bochenek et al. 2020) accompanied by simultaneous X-ray emission (Mereghetti et al. 2020; Tavani et al. 2021; Zhang et al. 2020b; Ridnaia et al. 2021). Whether magnetars or other sources (e.g., black holes, ultra-luminous X-ray sources) are considered as progenitors, multi-wavelength (MWL) emission is predicted by most models, in the form of a prompt or afterglow (see e.g., Beloborodov 2020, 2017; Lyutikov et al. 2020; Metzger et al. 2019; Ghisellini & Locatelli 2018; Kumar et al. 2017; Lyubarsky 2014). The detection of MWL emission from an FRB source would be an important piece of information to discriminate amongst the current models. A deep search for MWL emission was performed in the early days for FRB 20140514A (Petroff et al. 2015) and more than once for R1 (Hardy et al. 2017; Scholz et al. 2017, 2016).

The search for simultaneous emission at other wavelengths is better targeted in the case of a repeater, where we can expect to observe bursts during a MWL campaign. R1, however, is relatively far (~1 Gpc, Chatterjee et al. 2017; Marcote et al. 2017) and this has made the chances of detection with current optical and high-energy instruments slim. On the other hand R3, with its proximity (~149 Mpc, Marcote et al. 2020), as well as its periodic repetition, is a more suitable candidate for MWL coordinated observational campaigns. Indeed several were performed (Pearlman et al. 2020; Pilia et al. 2020; Scholz et al. 2020), however, with no MWL detections reported.

In this work, we present a MWL observational campaign on R3 conducted in the radio band with the Sardinia Radio Telescope (SRT) and the upgraded Giant Metrewave Radio Telescope (uGMRT) over the course of eight activity cycles of the source. Optical to γ-ray telescopes were used to shadow the radio observations and seek for higher energy emission. We report the detection of 21 radio bursts from the source and a null detection at other wavelengths, providing for the optical band and the high-energy stringent upper limits (ULs). The paper is organised as follows. Section 2 presents an overview of the instruments involved and the observing times and tools. Section 3 presents the detections in the radio band and the ULs at other wavelengths. In Sect. 4, we discuss our results. In Sect. 5, we provide our conclusions.

2. Observations and data reduction

We performed a MWL observing campaign on R3, focusing on different activity cycles, from 2020/10/23 to 2021/08/30. In this section, for each wavelength, we report the specifications of the instruments used and how the data have been processed. The whole campaign, with all the telescopes involved and the observing times, is summarised in Fig. 1.

2.1. Radio instruments

2.1.1. SRT

The SRT monitored R3 between 2020/11/09 and 2021/02/15, for a total observing time of ~39 h. The observations were made with the L/P dual band receiver (SRT-L and SRT-P, Valente et al. 2010), with observational central frequency of 1547 and 336 MHz respectively (see Table 1). The L-band data were recorded with the ATNF Digital Filterbank Mark III backend (DFB) whereas the P-band data were acquired via the ROACH1 backend (Bassa et al. 2016).

The L-band data were recorded as 2-bits per sample psr-fits (Hotan et al. 2004) search-mode files and subsequently con-

verted into 8-bits SIGPROC (Lorimer 2011) filterbank files; the P-band data, after being recorded as dada baseband files, are coherently dedispersed at dispersion measure (DM) = 348.82 pc cm^{-3} (CHIME/FRB Collaboration 2019b), to remove the intra-channel smearing, and converted into 8-bits filterbank files using the DSPSR (van Straten & Bailes 2011) routine digifil. The L-band receiver of 512 MHz bandwidth is divided into frequency channels of 1 MHz each and time sampled at 125 μs. The L-band data are originally recorded with a larger bandwidth of 1024 MHz to avoid aliasing effects. Radio frequency interference (RFI) typically affects less than 20% of the nominal 512 MHz band. The 80 MHz bandwidth of the P-band is split into 320 channels of 0.25 MHz each and sampled at 128 μs. The P-band bandwidth channels are generally corrupted by RFI for about 30%.

2.1.2. uGMRT

The uGMRT (Gupta et al. 2017) is an enhancement of the GMRT (Swarup et al. 1991) with improved receivers providing nearly seamless coverage from 50 to 1500 MHz and wide instantaneous bandwidths. The observations were carried out with the Band-3 receiver in the frequency range 300−500 MHz. The GMRT Wideband Backend (GWB, Reddy et al. 2017) was configured to split the 200 MHz bandwidth into 2048 spectral channels, giving a channel width of 97.65 kHz. At the time of the observation, the signals from 27 available antennas were combined in phase to give a phased array beam which was coherently dedispersed at DM = 348.82 pc cm^{-3}. The real-time coherent dedispersion corrects only for the intra-channel dispersion, while the inter-channel dispersion is expected to be corrected offline. The array was rephased every 20 min to undo the phase drift due to ionospheric effects on the far away arm antennas. The calibrator 3C48 was observed for a few minutes initially to provide the flux scale for fluence calibration in case of bursts detection. Custom total intensity raw data produced by the backend are then converted into 16-bits SIGPROC filterbanks[1]. The uGMRT observed R3 on 2021/08/15 for a total observing time of ~2.1 h.

2.1.3. Single pulse search

The search for radio bursts from R3 was performed using a search pipeline based on Heimdall (Barsdell et al. 2012). As a first step, an RFI excision is made using the spectral kurtosis algorithm (Nita & Hellbourg 2020) provided by the FRB software package YOUR (Aggarwal et al. 2020). The DM search was restricted to the range 300–400 pc cm^{-3}. For the SRT-P data, we chose a signal-to-noise ratio (S/N) loss tolerance in each DM trial of 1%. For the SRT-L and uGMRT data, we performed a sub-banded search (similarly to Kumar et al. 2021). In the case of SRT-L, the sub-banded search considered the full 1024 MHz dataset. In this way, the search for bursts was performed within the nominal 1300−1800 MHz, but we also took advantage of the fact that the receiver passband filter does not have a sharp drop at its edges and a non-negligible fraction of the signal of a putative band-limited burst could appear outside the nominal borders of the band.

We perfomed the sub-banded search by applying the following frequency windows: we took [512, 256] MHz windows (for each sub-band we took the overlapping adjacent sub-bands by shifting the bands by half widths) and we used a S/N tolerance
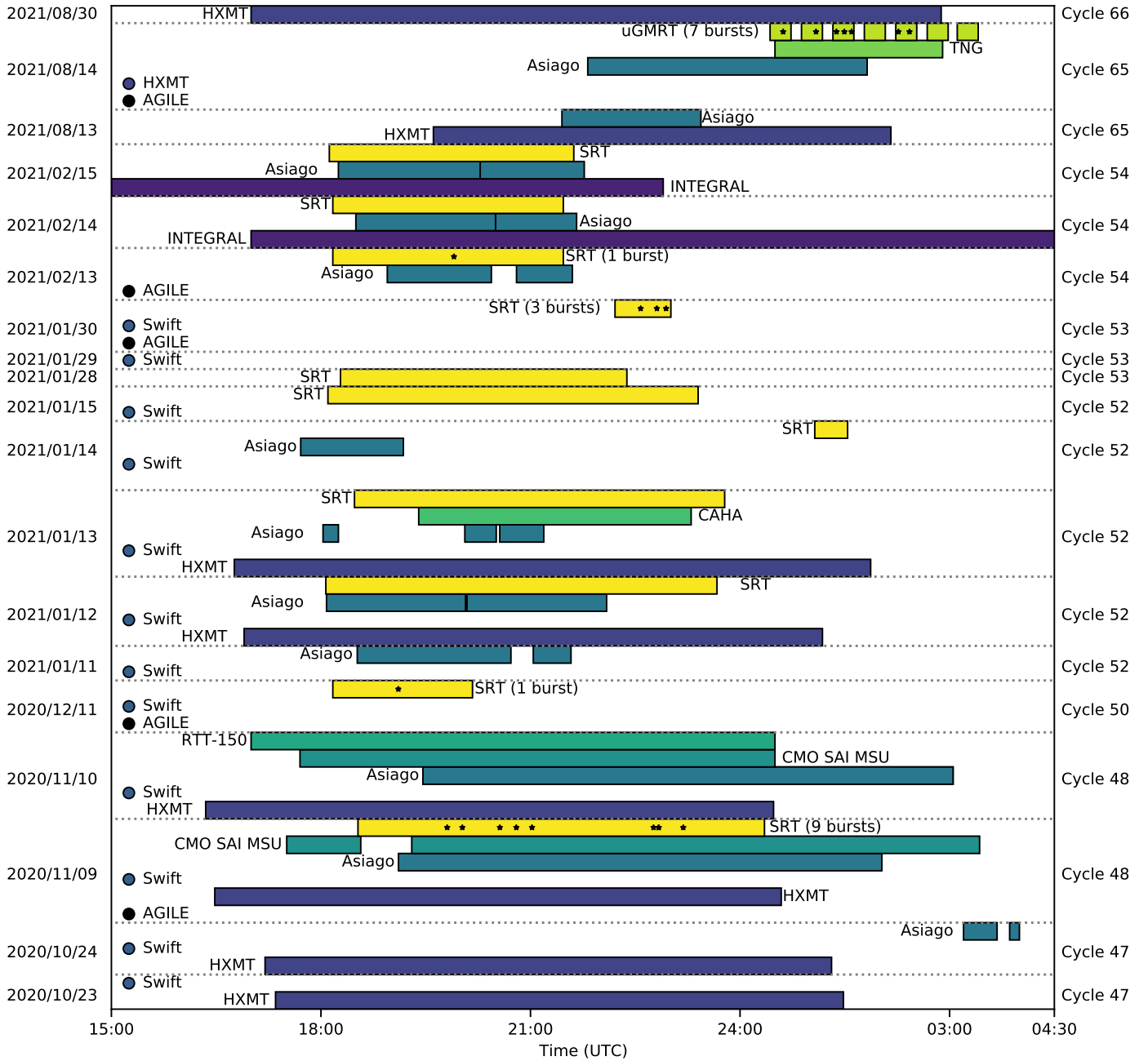
---

[1] https://github.com/alex88ridolfi/ugmrt2fil

Fig. 1. Observational R3 MWL campaign. Coloured bars represent observations performed for each facility as a function of time of the day (UTC). For each day (reported on the left), the corresponding activity cycle number of R3 is reported on the right. The time after 24:00 should be considered as part of the day after. Each detected radio burst is reported as a black star. AGILE and *Swift* (and *Insight*–HXMT on 2021/08/14) were observing throughout the whole day, except during epochs of visibility limitations (Earth occultations and South Atlantic anomaly passages). The days in which a single instrument is present are scheduled days in which observations with other instruments have been cancelled.

of [1, 0.1]% with respect to the previously mentioned sub-band widths. For the uGMRT data we considered windows of [200, 100] MHz and for each window a tolerance of [1, 0.5]%. In all the searches we used a maximum boxcar width of 500 ms.

In order to filter the high number of candidates found by `Heimdall` , we considered some thresholds to sift them using the code `frb_detector.py` (Barsdell et al. 2012). We selected only candidates with $S/N \geq 6$, and a minimum number of members (distinct boxcar/DM trial) clustered into a single candidate by `Heimdall` of 10. Lastly, all the candidates were visually inspected.

2.2. Optical Instruments

2.2.1. Asiago

Extensive optical coverage during periods of radio activity was attained with the fast photon counters Aqueye+ and IFI+Iqueye mounted at the *Copernicus* and *Galileo* telescopes, respectively, in Asiago (Zampieri et al. 2019, 2015; Naletto et al. 2009; Barbieri et al. 2009). The two instruments performed several observations of the area of the sky centered at the position of R3 (RA = $01^h58^m00^s\!.75017 \pm 2.3$ mas, Dec = $65°43'00''\!.3152 \pm 2.3$ mas, Marcote et al. 2020) at the dates reported in Table A.1

Table 1. Details of the radio instruments involved in the R3 MWL campaign.

Telescope	Receiver	ν_c [MHz]	BW [MHz]	dt [μs]	dν [kHz]	SEFD [Jy]	$F_\nu^{\min}$ [Jy ms]
SRT	L/P L-band	1547	512	125	1000	37	0.4
	L/P P-band	336	80	128	250	215	4.6
uGMRT	Band-3	400	200	81.92	97.65	$(502/N_A)$	0.6

Notes. For each instrument we report the central frequency ν_c, observational bandwidth BW, sampling time dt, spectral resolution dν, system equivalent flux density (SEFD) and the fluence density[a] threshold ($S/N = 6$) $F_\nu^{\min}$. N_A is the number of antennas deployed with the uGMRT array. [a]Throughout this work, we refer to the source irradiated energy per surface unit as the 'fluence', and to the fluence per frequency unit as the 'fluence density'.
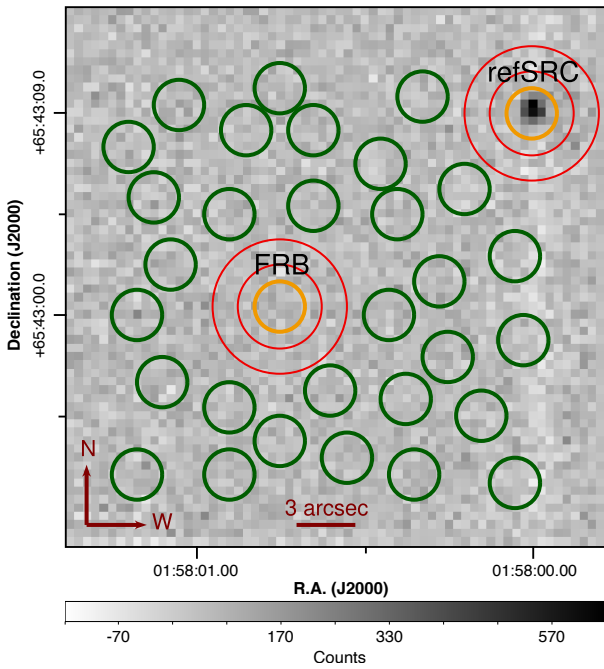

Fig. 2. Sum of twenty 5-ms frames collected by AstraLux. The R3 position and the reference field source are marked by orange circles. The rings where the background was computed are marked in red. In green the thirty random regions whose aperture photometry and count statistics were investigated.

(some of them are simultaneous). Observations were performed in white light. At the beginning and at the end of each acquisition, a reference star close to the position of the target (2MASS 01580548+6542269, offset 44″) was also observed to monitor the quality and transparency of the sky, namely, to check that the count rate was constant and consistent with the expected value (according to the calibration relations in Zampieri et al. 2016). The same star (for Aqueye+) or another field star (2MASS 01580026+6541437, for IFI+Iqueye) was selected and carefully centred on the instrument camera for guiding purposes, in such a way that the FRB position matches the aperture of the on-source detectors or the fiber position. To this aim, an image of the field was previously acquired and astrometrically calibrated. The error of the target position registered on the image is ~0.6″, significantly smaller than the aperture and/or fiber diameter.

The photon event lists were reduced using a dedicated software (QUEST v. 1.1.5, Zampieri et al. 2015). Light curves with different bins widths were computed from the reduced event lists and searched for any significant rate increase.

Periods of bad sky quality (count rate of the on-source detectors >3700 counts s^{-1} for Aqueye+ and >2600 counts s^{-1} for IFI+Iqueye) were discarded. The total useful on-source observing time was ~129.5 ks for Aqueye+ and ~62.1 ks for IFI+Iqueye (data discarded ~10−20%). The count rate averaged over all acquisitions was 3038 counts s^{-1} for Aqueye+ and 1282 counts s^{-1} for IFI+Iqueye.

2.2.2. CAHA 2.2m

The Calar Alto 2.2m telescope equipped with the AstraLux camera observed R3 for 3.3 h starting on 2021/01/13 19:24:25 UT. A GG 385 longpass filter was used (White ~667 ± 237 nm). AstraLux (Hormuth et al. 2008) uses an electron-multiplying, thinned, and back-illuminated 512 × 512 pixel CCD manufactured by Andor. It provides a field of view of 24″ × 24″ at a pixel scale of 47 mas pixel^{-1}. Using subarrays, binning, and short vertical shift times allows frame rates of more than 1 kHz. Operated as electron-multiplying CCD, as in the case of our observation, AstraLux can reach multiplication gains of up to 2500 with a linear response up to 70 photons per pixel.

Our observation was performed by applying a 8 × 8 binning (0.376″/pixel) and acquisition rate of 200 Hz, which gives 64 × 64 bin frames, 5 ms integration time each. Split into four observing blocks due to the constraints of the acquisition software, we accumulated a total of 2 360 000 frames. In order to include in the field of view the $G \simeq 15.6$ reference star located north-west of the FRB position, an offset of δRA ~ 8.8″ and δDec ~ −7.3″, with respect to the star, was applied to the pointing (see Fig. 2). The post-processing centre coordinates resulted to be RA = 01^{h}58^{m}00$\overset{s}{.}$60, Dec = 65°43′01″.4.

Custom software written in the IDL language was used to manage and analyse the custom AstraLux files. The procedure to identify a possible source onset consisted in aperture photometry at the FRB position, the mentioned reference field source and thirty additional 'void' regions, as shown in Fig. 2. A three pixel extraction radius (~1.2″) was adopted. Pointing drift was accounted for by monitoring the position of the reference source using 1-s accumulated images. The background was monitored in regions around the given positions (area of an external corona delimited by red circles in Fig. 2), whereas the bias level was computed from the average of the lower 12 rows of each frame to account for a variable, column-dependent variability. The frames' time-tagging precision is of the order of 0.1 s.

2.2.3. 2.5 m telescope CMO SAI MSU and 1.5 m RTT-150

We observed the position of R3 with the 2.5 m telescope of the Caucasian Mountain Observatory (CMO, Shatsky et al. 2020) of the Sternberg Astronomical Institute (SAI) Lomonosov Moscow

State University (MSU). We used the Andor iXon 897 camera mounted on Cassegrain focus. This allowed us to obtain 4 ms frames (with 0.28 ms readout time). No optical filter was used in order to maximise the sensitivity. Due to software limitations, the time tag was rounded to 1 s, thereby introducing a systematic error in the absolute timing. We selected a $80'' \times 20''$ field with two bright comparison stars with mean *Gaia G* magnitudes of 13.9 and 15.6: *Gaia* DR2 518385480138840704 and *Gaia* DR2 518386236053079936, respectively. The latter corresponds to the reference source observed by AstraLux. The angular scale after binning was $0.32''$/pixel.

We obtained about 14 h of useful exposure over the nights of 2020/11/09 and 2020/11/10, with single series duration of 1200 s. For each individual series an averaged image was produced and astrometric corrections, with respect to known *Gaia* stars, were performed. Then for each single frame of the series we once again corrected the position with respect to the brightest star in the field (which produced about 750 electrons above the noise level per frame). This allowed us to obtain a typical accuracy of the astrometric solution of $0.2''$.

Over the second night of 2020/11/10 we also performed simultaneous observations with the Andor iXon 888 camera mounted on the 1.5 m Russian-Turkish Telescope (RTT-150), accumulating about 6 h of data. No optical filter was used. We chose to select a single frame exposure of 8.24 ms with 0.1 ms readout time. The same two *Gaia* stars were used for astrometry. The expected noise signal distribution was acquired from the empty regions with no apparent stars in the field.

2.2.4. 3.6 m TNG

We carried out a single observation of R3 with the fast optical photometer SiFAP2 (Ghedina et al. 2018; Ambrosino et al. 2016) mounted at 3.6 m INAF's Telescopio Nazionale *Galileo* (TNG) located at Roque de Los Muchachos (La Palma, Canary Islands) on 2021/08/15. The observation was performed without any interruption starting at 00:35:00.000 UT and lasting 8.7 ks. No filter was used during the run to maximise the photon count rate. The final position of R3 (see Sect. 2.2.1) was reached by offsetting the telescope from GSC2.2 N31321329057 star (RA = $01^{\text{h}}58^{\text{m}}05.50$, Dec = $65°42'26''.87$) with a pointing error $<0''.5$, significantly better than the field of view of SiFAP2 ($7'' \times 7''$). The sky background located $\sim3.5'$ from the target was also monitored simultaneously with R3.

2.3. High-energy instruments

2.3.1. AGILE

The AGILE satellite observed the sky region in which R3 is located with its three detectors. The γ-ray imaging detector (GRID), sensitive in the range 30 MeV–30 GeV with a 2.5 sr field of view (FoV), a coded mask X-ray imager, Super-AGILE (Super-A; operating in the energy range 18–60 keV; Feroci et al. 2007) with $\sim$1 sr FoV, and the Mini-Calorimeter (MCAL), sensitive in the 0.4–100 MeV band with 4π non-imaging acceptance (Tavani et al. 2009; Tavani 2019). AGILE is currently operating in spinning mode, with the instrument axis rotating every $\sim$7 min around the satellite-Sun direction. For each satellite revolution, a large fraction of the sky ($\sim40-60\%$) is exposed, depending on the Earth occultation pattern and trigger disabling over the South Atlantic anomaly (SAA, about 10% of the 95-min orbit). In particular, on timescales of hours, $\sim80\%$ of the entire sky can be exposed by the GRID γ-ray imager and by the MCAL.

AGILE has been involved in the MWL campaigns for FRBs since 2019, particularly for R3 (Tavani et al. 2020; Casentini et al. 2020). The advantage to use an instrument like AGILE is closely related to its currently operating mode, the spinning. We are able to follow an FRB source minutes before and after each specific burst time with a small temporal gap. No evidence of γ-ray emission from these sources has been found so far (Verrecchia et al. 2021; Tavani et al. 2021). AGILE-GRID exposure near burst times has been checked on short timescales (±100 s around the bursts), and resulted in a partial coverage of the 21 bursts reported (only 12), due to SAA passages or Earth occultation. The long-timescale GRID analysis has been performed using the standard AGILE multi-source maximum likelihood (AML; Bulgarelli et al. 2012), usually applied to exposures longer than a few hours. We applied standard cuts to events, excluding SAA passages time intervals and events at off-axis angles greater than 60 deg or at angles from Earth direction smaller than 80 deg.

2.3.2. *Insight*–HXMT

Insight–HXMT is China's first X–ray astronomy mission (Zhang et al. 2020a). It is equipped with three main X–ray instruments operating in the broad 1–250 keV band: the Low Energy (LE) X–ray telescope covers the 1–15 keV band (Chen et al. 2020); the Medium Energy (ME) instrument covers the 5–30 keV band (Cao et al. 2020); and the 20–250 keV band is covered by the High Energy (HE) instrument (Liu et al. 2020). The time resolution of the LE, ME, and HE are 980 µs, 255 µs, and less than 10 µs, respectively. The systematic errors of the timing system are 15.8, 8.6, and 12.1 µs, for LE, ME, and HE, respectively (Tuo et al. 2022).

While the general procedure we followed to extract the light curves is the same as detailed in Guidorzi et al. (2020), in order to increase the exposure coverage of the observations we lifted some of the standard constraints employed to determine the good time intervals (Li C.-K. and Ji Long, personal communication). In particular, the only constraints passed to the `legtigen`, `megtigen` and `hegtigen` tasks were: Earth elevation angle ELV > 1 deg for LE and ME, ELV > 0° for HE; the pointing offset angle ANG_DIST $\leq 0.5°$ for HE. For all three instruments, the SAA_FLAG (excluding the data in the SAA) was set to false.

The effect of this non-standard procedure is to not filter the data for high background regions. Because our pipeline estimates the background independently (Guidorzi et al. 2020), this does not affect our results. The advantage, on the other hand, is to cover a much larger time exposure, therefore increasing significantly the chance to find bursts.

The *Insight*–HXMT data analysis was performed with the software package HXMTDAS v2.04 and CALDB v2.05. We used the `hxbary` to apply the barycentric correction, thus converting the photons' arrival terrestrial times (TTs) to the corresponding barycentric dynamic times (TDBs). LE, ME and HE instruments total on source exposure was of 127.7, 118.8 and 80.3 ks respectively. Table A.4 reports the observation log.

2.3.3. INTEGRAL

In total, between October 2020 and August 2021, INTEGRAL observed R3 for 658.0 ks (8.0 days) in 276 pointings. All of these data are currently public. INTEGRAL observations consist of approximately 1-hour-long pointings (binned at 1 s resolution), with a few hundred seconds slews in between. For the purposes

of the observation log, we group them into longer observations, as long as the pointings are separated by no more than 300 s, as reported in Table A.5. The INTEGRAL data analysis has been conducted by using the standard INTEGRAL Offline Scientific Analysis software (version 11.0).

2.3.4. *Swift*

The *Neil Gehrels Swift* Gamma-ray Burst Observatory (*Swift*) observed R3 with the X-ray Telescope (XRT, Burrows et al. 2005), one of the three instruments carried by the facility. The *Swift*/XRT data were obtained within the planned coordinate multi-instrument campaign started in 2020 whose first results have been partially reported in (Tavani et al. 2020, 2021). We monitored R3 in the X-rays (0.3–10 keV) daily during 15 activity cycles (12 of them falling within the time intervals of this work). The XRT observations were carried out in windowed timing (WT) readout mode, with 2–7 daily pointings. The time resolution of WT data is 1.8 ms and each pointing has a typical exposure of ∼1.8 ks. We combined all the data within each proposal and processed them using the XRTDAS software package (v.3.7.0)[2] within the HEASoft package (v.6.30.1). The data were calibrated and cleaned with standard filtering criteria using the xrtpipeline task and the calibration files available from the *Swift*/XRT CALDB (version 20220803). The imaging analysis was executed selecting events in the energy channels between 0.3 and 10 keV and within a 20 pixel (∼47″) radius, including the 90% of the point-spread function. The background was estimated from a nearby source-free circular region with the same radius value.

3. Results

3.1. Radio

3.1.1. Properties of bursts

Throughout the whole campaign the radio instruments, SRT and uGMRT, detected a total of 21 bursts (14 from the SRT at *P*-band and seven with the uGMRT). Figures 3 and 4 show the dedispersed (DM = 348.82 pc cm^{-3}) waterfall plots of the bursts. Their properties are reported in Table 2.

The widths of the bursts were computed as the full width at half maximum of a Gaussian function. In the case of the SRT, the data have been converted into flux density units applying the standard radiometer equation (Lorimer & Kramer 2005). In the case of uGMRT (as mentioned in Sect. 2.1), we calibrated the FRB data by multiplying it with a conversion factor counts-Jy estimated via on-source and off-source observations of 3C48 (Perley & Butler 2017). The fluence densities F_ν were computed by integrating the calibrated background subtracted light curves within their respective burst widths.

The bursts detected by both radio telescopes do not possess complex structure, apart from the of SRT-P-05 and uGMRT-03 in which two sub-bursts are present, with the latter not clearly resolvable. Six of the 21 bursts show a downward drifting toward lower frequencies, as already seen from this source (Chawla et al. 2020; Chamma et al. 2021). We evaluated the linear drift rate $\dot{\nu}$ by using a standard auto-correlation analysis (Hessels et al. 2019), obtaining values which scatter around an average value of -10 ± 1 MHz ms^{-1} for the four bursts of SRT-P and -8.2 ± 0.8 MHz ms^{-1} for the two bursts from uGMRT.

---

[2] Developed by the ASI Space Science Data Center (SSDC).

3.1.2. *L*-band observations and frequency-dependent activity of R3

Regarding the SRT *L*-band, in addition to the standard single-pulse search, we carefully inspected the data for clustered bright pixels located ∼9.9 s (the DM-delay between the top-frequencies of SRT-L and SRT-P) before the bursts at *P*-band. We do not report any occurrence of a burst that was simultaneous at two different radio frequencies, as already noticed for R3 by Sand et al. (2022), Pilia et al. (2020). This is similar to what was observed for R1 (Majid et al. 2020; Caleb et al. 2020) although, interestingly, R1 was multi-band simultaneously detected once (Law et al. 2017). For the whole campaign, by exploiting the radiometer equation, we set a fluence density UL (for a $S/N = 6$, 1 ms burst) of about 0.4 Jy ms at *L*-band. At *P*-band, for the dates in which we had no detection, we set a fluence density UL of about 4.6 Jy ms.

Table 2 shows the bursts phases (ϕ), obtained by folding the time of arrivals (TOAs) at $P = 16.33$ days and reference epoch of 58369.40 MJD (Pleunis et al. 2021). The SRT bursts at 336 MHz have phases within the range of $0.46 < \phi < 0.62$, while all the uGMRT bursts have $\phi \sim 0.62$ as they were detected on the same day. Figure 5 shows the number of bursts detected and the telescope exposure time as a function of the activity phase ϕ. Since we only observed with the uGMRT for a single day, we only discuss the SRT case. In addition to our burst sample, we include the three bursts published by Pilia et al. (2020), which were observed with the SRT using the same dual-band receiver (for a total observing time of ∼30 h) and detected at *P*-band. The SRT observations span a phase range $0.46 < \phi < 0.72$, with a total observing time of 69 h distributed for ∼40% in $0.46 < \phi < 0.56$, ∼37% in $0.56 < \phi < 0.66$, and ∼23% in $\phi > 0.66$. 70% of our detections lie in the second phase range, with the rest being in the first one, which suggests that our low-frequency detections follow the frequency-dependent activity manifested by R3 (see Sect. 1).

We compared our detections to those reported by CHIME in Pleunis et al. (2021; 54 detections) at 600 MHz and with the LOFAR bursts (26 bursts, Pleunis et al. 2021; Pastor-Marazuela et al. 2021) at 150 MHz. From the top panel of Fig. 5, which depicts the number of detections normalized by the exposure time (i.e. the rate), we see that the SRT-P distribution appears compatible with both CHIME and LOFAR. To investigate whether our bursts are drawn from the same distributions as the one of the CHIME or LOFAR bursts, we performed a two-sample Anderson-Darling test (AD, see e.g., Scholz & Stephens 1987). By applying the AD test on the SRT-P/CHIME (SRT-P/LOFAR) dataset, we obtain a confidence level of only 2.8σ (1.6σ) indicating that the SRT-P bursts may not be drawn from the same distribution as CHIME (LOFAR). Based on these results, we conclude that our burst distribution, given the current dataset, is compatible with both CHIME and LOFAR, and further detections are necessary to expand on these results.

Our non-detections at *L*-band are consistent with the chromatic activity of R3, given the covered phase ranges, even though detections have been recorded at phases up to $\phi = 0.5$ (Pastor-Marazuela et al. 2021). Furthermore, our observations at *L*-band were performed with a channel width of 1 MHz, which retains an intra-channel smearing of ∼0.7 ms.

Shorter bursts would have potentially been lost. Our non-detections are, again, consistent with the observed properties of R3 bursts, given that the bursts detected at higher frequencies (>1 GHz, Bethapudi et al. 2022; Pastor-Marazuela et al. 2021) have smaller temporal widths ($\lesssim 1$ ms), comparable with our

Table 2. Properties of the detected bursts.

Burst ID	TOA [MJD]	ϕ	Δt [ms]	S_ν [Jy]	F_ν [Jy ms]	E [10^{37} erg]	$\dot{\nu}$ [MHz ms^{-1}]
SRT-P-01	59162.8253243218	0.5870	19 ± 2	3.1 ± 0.8	48 ± 16	8 ± 2.5	N.A.
SRT-P-02	59162.8343320911	0.5875	14.0 ± 0.5	12.2 ± 3.0	139 ± 43	24 ± 7	-9.7 ± 0.6
SRT-P-03	59162.8567440946	0.5889	13.2 ± 0.5	11.7 ± 2.9	125 ± 39	21 ± 6	-11.4 ± 0.6
SRT-P-04	59162.8665428914	0.5895	23 ± 2	3.2 ± 0.8	61 ± 20	10 ± 2	N.A.
SRT-P-05	59162.8752448474	0.5900	18 ± 2	5.3 ± 1.5	77 ± 29	13 ± 3	N.A.
	59162.8752449374	0.5900	23 ± 1	5.3 ± 1.5	98 ± 27	17 ± 3	N.A.
SRT-P-06	59162.9481096844	0.5945	14 ± 2	5.5 ± 1.4	62 ± 23	10 ± 6	N.A.
SRT-P-07	59162.9513861530	0.5947	23 ± 4	2.7 ± 0.7	50 ± 20	8 ± 1	N.A.
SRT-P-08	59162.9515615864	0.5947	20 ± 2	3.0 ± 0.7	49 ± 17	8 ± 1	N.A.
SRT-P-09	59162.9661486339	0.5956	12 ± 2	2.3 ± 0.6	22 ± 9	4 ± 3	N.A.
SRT-P-10	59194.7961833830	0.5448	9 ± 2	2.1 ± 0.6	15 ± 7	3 ± 1	N.A.
SRT-P-11	59244.9407380909	0.6155	22 ± 2	5.2 ± 1.3	92 ± 21	16 ± 2	-11.3 ± 0.6
SRT-P-12	59244.9503715983	0.6160	18.1 ± 0.9	11.8 ± 2.9	172 ± 55	29 ± 6	-10.7 ± 0.6
SRT-P-13	59244.9559004303	0.6164	12 ± 1	7.3 ± 1.9	70 ± 27	12 ± 3	N.A.
SRT-P-14	59258.8293625230	0.4660	16 ± 2	4.9 ± 1.3	64 ± 23	10 ± 2	N.A.
uGMRT-01	59441.0257263218	0.6231	20 ± 2	0.8 ± 0.2	8.9 ± 0.8	2.1 ± 0.2	-5.9 ± 0.5
uGMRT-02	59441.0453208005	0.6243	9.2 ± 0.7	0.6 ± 0.2	2.8 ± 0.9	0.3 ± 0.1	N.A.
uGMRT-03	59441.0575323455	0.6250	20.8 ± 0.6	7.9 ± 0.2	84 ± 3	36 ± 1	-10.5 ± 0.5
uGMRT-04	59441.0622128892	0.6254	7.6 ± 0.8	0.4 ± 0.4	2.5 ± 0.7	0.6 ± 0.1	N.A.
uGMRT-05	59441.0665624511	0.6256	6 ± 1	0.4 ± 0.1	0.6 ± 0.1	0.06 ± 0.01	N.A.
uGMRT-06	59441.0944839544	0.6273	16 ± 4	1.3 ± 1.2	7.9 ± 2.3	0.8 ± 0.2	N.A.
uGMRT-07	59441.1011067833	0.6277	15 ± 8	0.2 ± 0.1	0.9 ± 0.8	0.2 ± 0.2	N.A.

Notes. The second column reports the barycentric time of arrival (TOA) at infinite frequency (TDB units, DE405 ephemeris, TAI clock, DM-delay constant 2.41×10^{-16} pc cm^{-3} s, reference frequencies for the DM correction are 375.875 MHz for SRT-P and 500 MHz for uGMRT). The TOAs have been computed via the Tempo2 software (Hobbs et al. 2006). The third column contains the bursts phase ϕ (see Sect. 3.1.2). The fourth column reports the FWHM width Δt of the bursts. S_ν, F_ν, E are respectively the peak flux density, the fluence density and the isotropic energy of the bursts. The last column reports the linear drift rate $\dot{\nu}$ of the bursts (for the bursts for which it was not possible to assess this value, i.e. a drift was not present, a N.A. value is reported).

smearing, with respect to those at frequencies of a few hundred MHz, which have widths of the order of tens of milliseconds (Pastor-Marazuela et al. 2021).

3.1.3. Source activity rate

Of the 14 SRT detections, 9 took place on the same day. We observed R3 for 5.8 h on 2020/11/09, implying an average burst rate of ~ 1.55 h^{-1} at the SRT-P frequencies and above a fluence density of 4.6 Jy ms. This value seems particularly high when compared, for instance, to the 2021/02/13 observation, where we observed the source for 2 h and detected only one event (corresponding to a burst rate of 0.5 h^{-1}). In order to assess if the 2020/11/09 was a highly active day, as it frequently happens for R1 (Zhang et al. 2018; Li et al. 2021; Hewitt et al. 2022; Jahns et al. 2023), we follow arguments similar to those discussed by Trudu et al. (2022) to obtain the rate of events expected by the SRT-P. We scale the rate reported for the source by CHIME/FRB of $R_0 = 0.9 \pm 0.5$ h^{-1} at 600 MHz and above a fluence density of 5.2 Jy ms (CHIME/FRB Collaboration 2020) to the SRT-P central frequency and fluence density limit. We consider a value of $\beta = 1.5$ (Macquart et al. 2019) as the spectral index and a slope $\alpha = 2.3$ (CHIME/FRB Collaboration 2020) for the cumulative fluence distribution $N(>F) \propto F^{-\alpha+1}$ obtaining:

$$R(>F_\nu) = R_0 \times \zeta(\text{BW}, F_\nu^{\min}) \times \left(\frac{\nu_c}{600 \text{ MHz}}\right)^{-\beta} \times \left(\frac{F_\nu}{5.2 \text{ Jy ms}}\right)^{-\alpha+1}.$$
(1)

Here, we additionally introduced a coefficient $\zeta(\text{BW}, F_\nu^{\min})$ to take into account the observational biases of the bandwidth BW of SRT-P to detect off-band events above its fluence density threshold $F_\nu^{\min}$ as discussed by Aggarwal (2021). We estimated $\zeta(\text{BW}, F_\nu^{\min})$ via a Monte Carlo simulation. We modeled a burst from R3 as a Gaussian function in the frequency domain with the amplitude (energy), the frequency centroid and the FWHM width as free parameters. We assumed the energy distributed in the range $(10^{36}-10^{40})$ erg as a negative power-law with the same index α. The frequency centroids were drawn from a uniform distribution $\mathcal{U}(300, 1000)$ MHz. We excluded the LOFAR frequencies and frequencies >GHz to avoid to add to the model the frequency-dependent activity of the source (see Sect. 3.1.2). Lastly, the FWHM frequency widths were assumed to be normal-distributed $\mathcal{N}(\mu, \sigma)$, with a mean value of $\mu = 107$ MHz and standard deviation of $\sigma = 59$ MHz. We obtained them by considering the reported R3 frequency widths by CHIME/FRB (Mckinven et al. 2023; Pleunis et al. 2021; CHIME/FRB Collaboration 2020, 2019b): with its 400 MHz observational bandwidth, it provides the least biased frequency width measurements. We generated 1000 bursts and evaluated ζ as the fraction of these generated bursts which are detectable by the telescope (hence, being above the telescope fluence density threshold), and repeated this for 1000 trials. In doing so, we obtained a result of $\zeta(80 \text{ MHz}, 4.6 \text{ Jy ms}) = 0.33 \pm 0.04$ for the SRT-P. Including all these parameters, Eq. (1) yields a burst rate $R(>4.6 \text{ Jy ms}) = 0.7 \pm 0.4$ h^{-1} for SRT-P, implying that the 2020/11/09 and 2021/02/13 rates were not outliers.
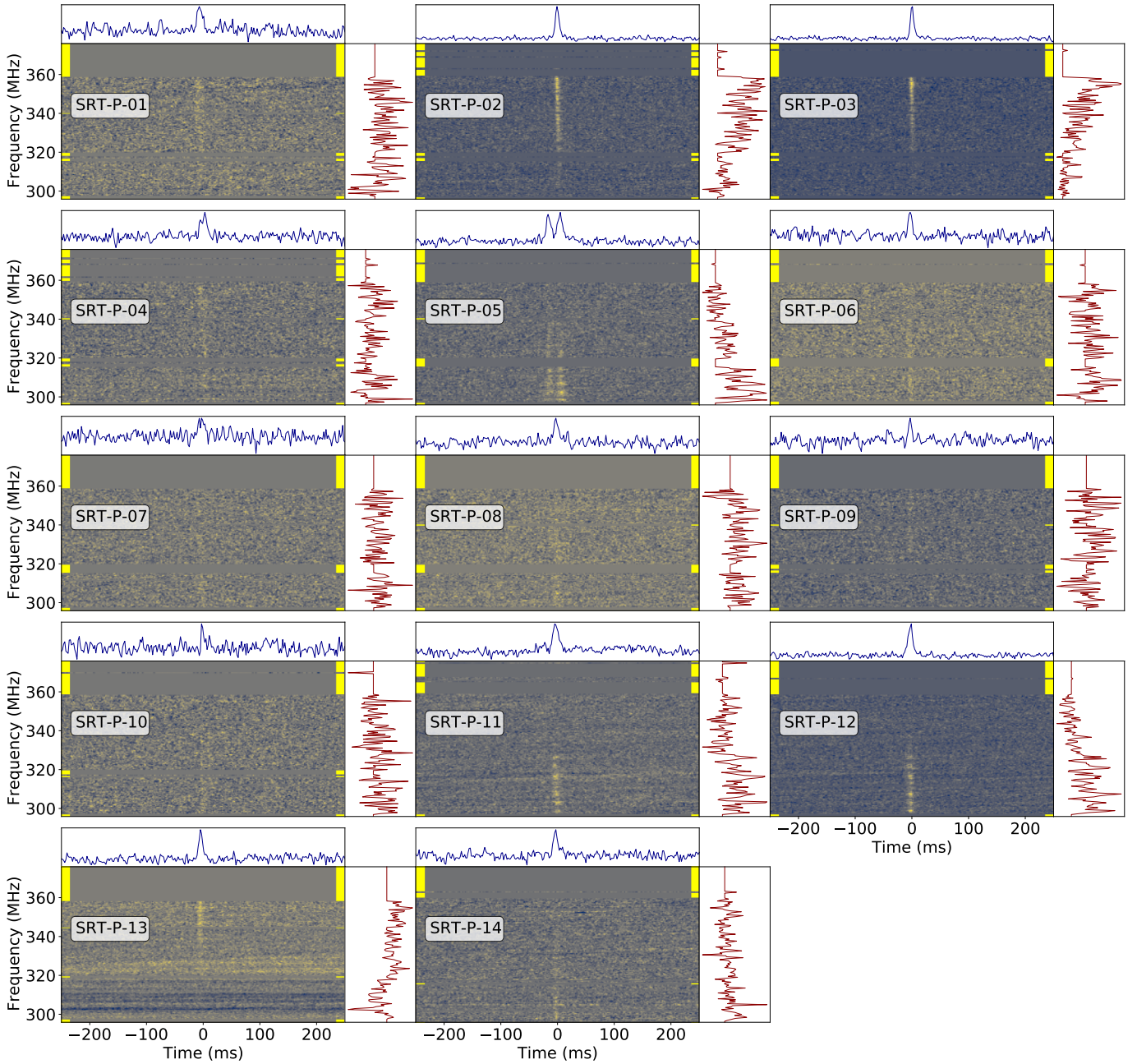
Fig. 3. Bursts detected with the SRT. The data have a resolution of 0.5 MHz in frequency and 1.9 ms in time. For each burst, the top panel shows the frequency-averaged time series. The central panel is the spectrogram of the signal and the right panel is the time averaged (around the width of the burst) spectrum. The rows with the yellow ticks are masked channels due to RFI.

3.2. Optical

3.2.1. Asiago

We performed a search for any significant increase in the count rate on the 1 ms binned optical light curves of all acquisitions and, in particular, around the time of the detected radio bursts. All nine bursts detected with SRT in 2020/11/09, the single burst detected in 2021/02/13 and the seven bursts detected with uGMRT in 2021/08/14 fall inside Aqueye+ and/or IFI+Iqueye observing windows. The acquisitions of 2021/08/14 were contaminated by the activity of the Perseid meteor shower.

To assess the significance of a peak, we followed the procedure adopted by Zampieri et al. (2022) to search for optical bursts at the time of the occurrence of hard X-ray burst

from the magnetar SGR J1935+2154. We assume a Poisson distribution with the average rate of the observation and fix a 3σ detection threshold $n_{t,obs}$ corresponding to a chance probability of $0.0027/N_{trials}$ in any of the bins of the observation. In case a radio burst is detected, we calculate also a detection threshold n_t corresponding to a chance probability of $0.0027/N_{trials}$ in any of the bins during an interval of ±100 ms and ±15 s around the time of arrival of the burst. These two values were chosen to estimate the significance in the two different scenarios of an optical burst almost coincident with the radio burst, and a delayed one. N_{trials} is the total number of bins in the interval. We obtain typical values of $n_{t,obs}$ in the range 18–20 counts bin^{-1} for Aqueye+ and 12–14 counts bin^{-1} for IFI+Iqueye. For the observations in which radio bursts
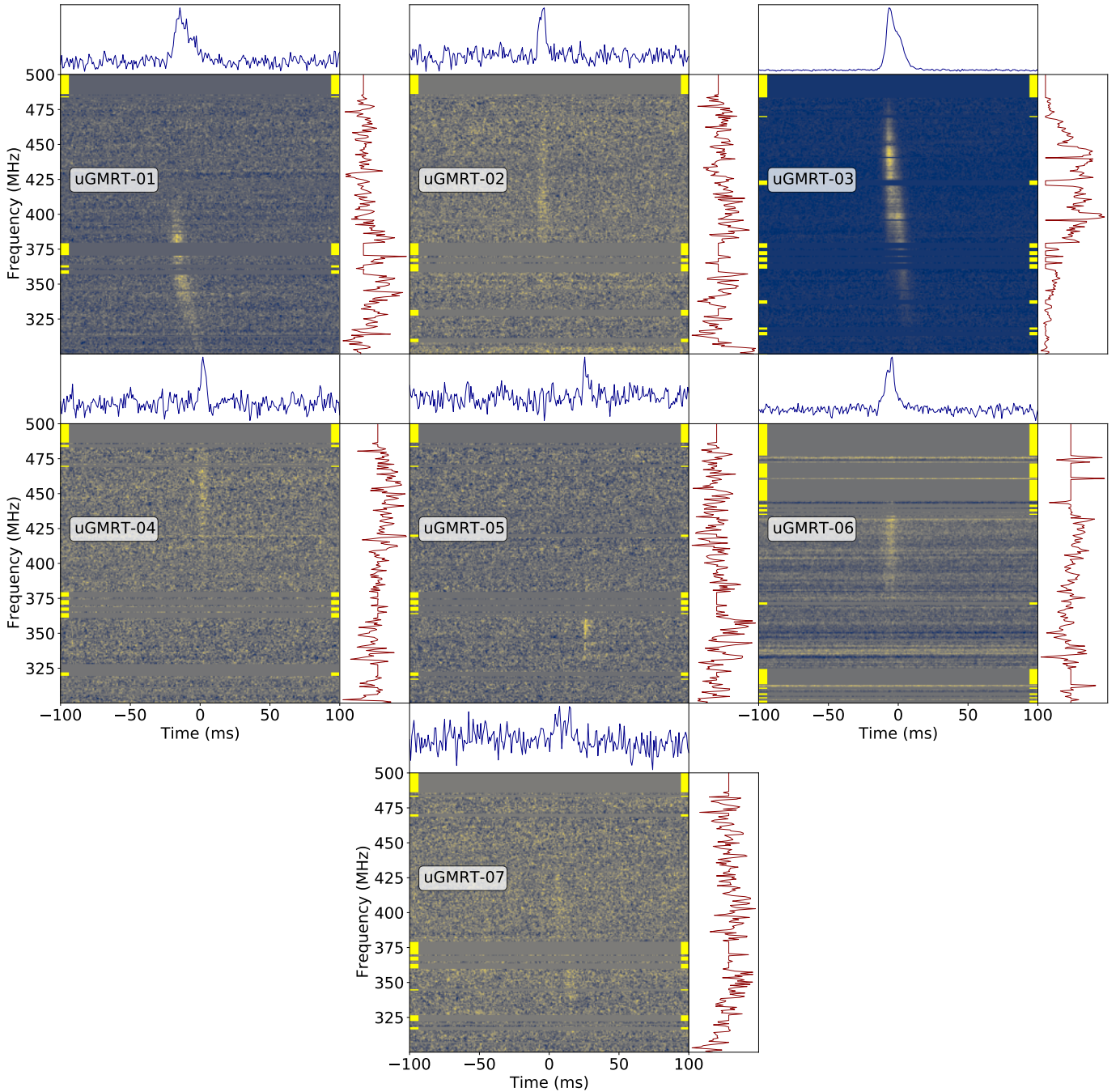
Fig. 4. Bursts detected with the uGMRT. The data have a resolution of 0.8 MHz in frequency and 0.8 ms in time. For each burst, the top panel shows the frequency-averaged time series. The central panel is the spectrogram of the signal and the right panel is the time averaged (around the width of the burst) spectrum. The rows with the yellow ticks are masked channels due to RFI.

were detected, we obtain $n_t(100\,\text{ms}) = 11\text{–}13\,\text{counts bin}^{-1}$ and $n_t(15\text{s}) = 15\text{–}16\,\text{counts bin}^{-1}$ for Aqueye+ (2020/11/09 and 2021/08/14; see Table A.1) and $n_t(100\,\text{ms}) = 6\text{–}8\,\text{counts bin}^{-1}$ and $n_t(15\,\text{s}) = 10\text{–}11\,\text{counts bin}^{-1}$ for IFI+Iqueye (2020/11/09 and 2021/02/13, see Table A.1).

Only one on-source optical peak with $n = 18\,\text{counts bin}^{-1}$ in an Aqueye+ observation falls within an interval of $\pm 15\,\text{s}$ around the SRT-P-02 TOA. In barycentred time units, the optical leads the radio one by $13.971\,\text{s}$ (see Fig. 6). This peak is slightly above threshold for the $\pm 15\,\text{s}$ window ($n_t = 15\,\text{counts bin}^{-1}$), corresponding to a potential detection at the 90% confidence level of an optical burst with $14.4\,\text{mag per ms}$, a fluence den-

sity of $0.007\,\text{Jy ms}$, and a luminosity of $1.6 \times 10^{43}\,\text{erg s}^{-1}$), but slightly below threshold considering the entire observation ($n_{t,\text{obs}} = 19\,\text{counts bin}^{-1}$). In fact, two other peaks are detected in the same observation, each with $n = 17\,\text{counts bin}^{-1}$. We thus conclude that this optical flash is marginally significant, but it is not at a high enough level to consider it a robust counterpart of the radio burst.

To estimate an UL to the optical brightness during a radio burst, we considered the highest on-source-only peak occurring in an interval of $\pm 100\,\text{ms}$ and $\pm 15\,\text{s}$ around the time at which a burst is detected, after subtracting a rate per bin that has a high Poissonian probability (99.73%) to be
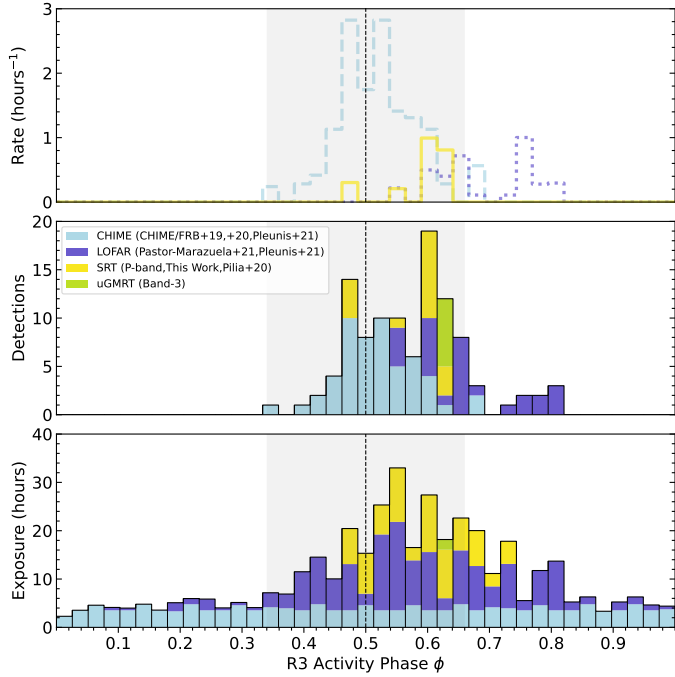
Fig. 5. Number of burst detections (mid panel), exposure time (bottom panel) and events rate (top panel) as a function of the activity phase of R3 both for the SRT and the uGMRT. Data from CHIME (Pleunis et al. 2021; CHIME/FRB Collaboration 2020, 2019b) and LOFAR (Pleunis et al. 2021; Pastor-Marazuela et al. 2021) are reported as a comparison. The grey area depicts the CHIME predicted activity window.

exceeded by chance in a single bin. This procedure returns an UL of 7–10 counts bin^{-1} (in ±100 ms) and 12–16 counts bin^{-1} (in ±15 s) for the two Aqueye+ observations of 2020/11/09 and 7–9 counts bin^{-1} (in ±100 ms) and 11–14 (in ±15 s) for the Aqueye+ observation of 2021/08/14. Using the V band calibration of Aqueye+ (Zampieri et al. 2016), these values correspond to an average (non extinction corrected) optical brightness of $V_{\pm100\mathrm{ms}}$ 14.25–14.64 mag per ms and $V_{\pm15\mathrm{s}} =$ 13.74–14.05 mag per ms for 2020/11/09 and $V_{\pm100\mathrm{ms}} =$ 14.49–14.64 mag per ms and $V_{\pm15\mathrm{s}} =$ 13.88–14.15 mag per ms for 2021/08/14. The corresponding deepest non extinction-corrected upper limits to the fluence density are: 4.6×10^{-15} erg cm^{-2} (0.005 Jy ms) for an interval of ±100 ms and 7.9×10^{-15} erg cm^{-2} (0.009 Jy ms) for an interval of ±15 s in November 2020; 4.6×10^{-15} erg cm^{-2} (0.005 Jy ms) for an interval of ±100 ms and 7.2×10^{-15} erg cm^{-2} (0.008 Jy ms) for an interval of ±15 s in August 2021. Assuming a distance of 149 Mpc (Marcote et al. 2020), these values eventually imply the following limits to the luminosity: 1.2×10^{43} erg s^{-1} for an interval of ±100 ms and 2.1×10^{43} erg s^{-1} for an interval of ±15 s on 2020/11/09; 1.2×10^{43} erg s^{-1} for an interval of ±100 ms and 1.9×10^{43} erg s^{-1} for an interval of ±15 s on 2021/08/14.

The lack of detection of any optical peak during the partially simultaneous observations of 2020/11/09 with IFI+Iqueye confirms these results, although the inferred ULs are less deep. IFI+Iqueye was the only active optical photometer in 2021/02/13, at the time of the SRT detection of SRT-P-14 (obs ID 20210213-195451; see Table A.1). The UL inferred for this observation are 7 counts bin^{-1} in ±100 ms and 10 counts bin^{-1} in ±15 s that, using the V band calibration of IFI+Iqueye (Zampieri et al. 2016) and the overall optical transmission efficiency at the time of the observation (32%), corresponds to

an average (non extinction corrected) optical brightness of $V_{\pm100\mathrm{ms}} = 11.6$ mag $V_{\pm15\mathrm{s}} = 11.2$ mag. The corresponding ULs to the fluence density are 7.9×10^{-14} erg cm^{-2} (0.09 Jy ms) and 1.1×10^{-13} erg cm^{-2} (0.13 Jy ms), respectively.

On the other hand, significant optical peaks of duration between ~1 ms and ~10 ms are detected during some observations. While some are simultaneously observed with the on-source and sky detectors and are therefore diffuse foreground atmospheric events (most likely meteors), others are on-source-only or sky-only events the nature of which is still under investigation. Results of this analysis will be reported elsewhere.

3.2.2. CAHA 2.2 m

The $\simeq2.4$ million 5-ms frames collected by CAHA 2.2 m/AstraLux on 2021/01/13 were initially investigated for events deviating by more than 5σ from the background. We performed aperture photometry at the FRB position after removing frames affected by multi-pixels cosmic rays, which were not automatically filtered out by the analysis software. A conservative 6σ level cut allowed us to identify a total of 28 candidate events. To quantify the statistical significance of this value, we performed the same analysis on the thirty void regions shown in Fig. 2. The resulting number of candidates was similar.

As a cross-check, the light curves obtained summing the counts collected on the FRB, void, and reference source regions were statistically investigated. As expected, the distribution of net counts (centre $\simeq 4200$, $\sigma = 2130$) and the corresponding σ for the $G \simeq 15.6$ reference source clearly show its detection (see Fig. 7). In fact, the 1-s integrated light curve shows no sign of variability. On the other hand, for the FRB and void regions, the bias-subtracted count distributions are zero-centred and narrower ($\sigma \sim 1400$). However, we note that only one or two values exceed the 6σ level (~10–15 above 5σ). This is quite different from the figures obtained by the aperture photometry. A visual inspection of the frames with $\sigma > 6$ at the FRB location revealed two cases that we can consider of interest, occurring at 19:47:29.7 and 22:29:50.9 UTC. However, lacking a simultaneous monitoring with any other instrument, we cannot claim a burst detection. Based on the overall statistics of the reference source, we quote a limiting magnitude (white filter, not corrected for extinction) for the single 5 ms frame of 16.0 at 3σ and 15.5 at 5σ. The latter corresponds to an upper limit on the putative source luminosity of 5.3×10^{42} erg s^{-1}.

3.2.3. CMO SAI MSU and RTT-150

Over two nights, we accumulated about 12 million frames on the 2.5 m CMO telescope. For each frame, we estimated the signal in a 2.5″ (radius) aperture around the FRB position and also the background level in several selected regions. The mean signal in aperture was 20 electrons. Assuming a Poisson distribution for the signal with this mean value, the standard deviation is 4.4 electrons. The probability to have more than one frame with signal larger than 48 electron from background in series of 1.2×10^7 frames is 0.37. We performed a search for flux excursions with this threshold on individual frames. After a manual screening of the selected frames (which were caused by cosmic rays and detector anomalies), no viable candidate bursts was left. Assuming a linear response of the camera we could place a conservative UL on optical emission from the FRB position at a level of 16.5 G magnitude per 4 ms frame. Taking into account the fact that the normalised response curve of our instrument deviates from the *Gaia G* band response curve by no
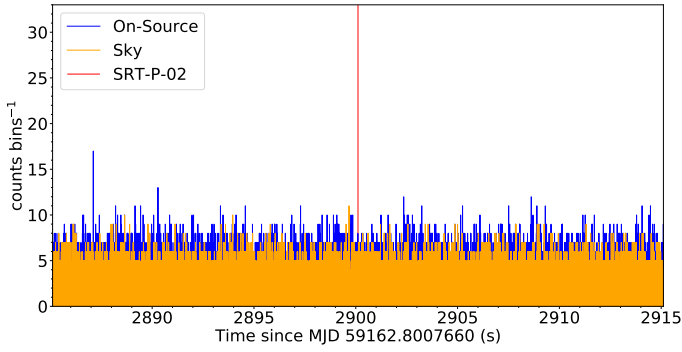
Fig. 6. Light curves (binned at 1 ms) of the on-source (blue) and sky (orange) detectors of the Aqueye+ observation corresponding to R3, taken on 2020/11/09 (Obs ID 20201109-200635 in Table A.1, the Aqueye+ starting time has been barycentred). An interval of ±15 s around the time of arrival of the burst SRT-P-02 (red vertical line) is shown.
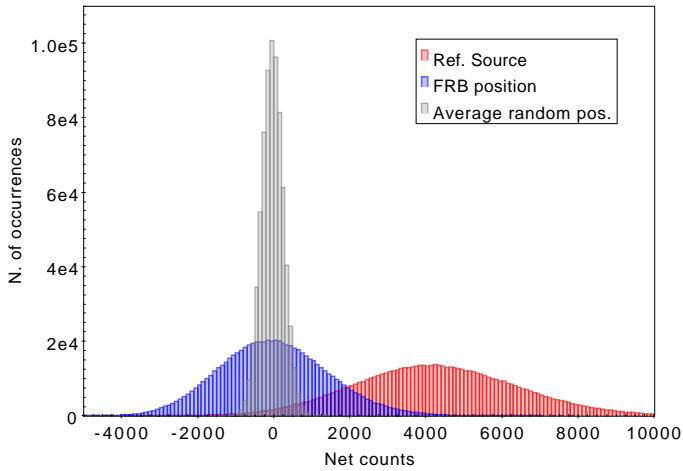

Fig. 7. Count statistics comparison at the FRB (blue) and reference source (red) position. The grey histogram is obtained averaging the counts from the thirty random regions reported in Fig. 2. Here, we plot the initial 720 000 net counts from the 5-ms frames collected by AstraLux.

more than 11%, we can put constraints on the mean flux density: 8.9×10^{-16} erg s^{-1} cm^{-2} Å^{-1}.

A similar analysis to the one described above was performed over the RTT-150 data. Apart from a few large amplitude outliers caused by the cosmic rays or CCD glitches no viable candidate events were found, providing an 5σ UL of about 15.5 G magnitude.

3.2.4. TNG

Seven bursts were detected by the uGMRT during the observation carried out on the night of 2021/08/14 (see Table 2) during which SiFAP2/TNG was observing for about 70% of the total radio exposure time. As in the case of Asiago simultaneous observation (see Sect. 3.2.1 for more details), also our data were affected by the Perseid meteor shower, causing several high-significance spikes to be randomly distributed within the dataset of SiFAP2. We detected them on both detectors of SiFAP2 monitoring the target and nearby sky background, respectively (see Sect. 2.2.4). To search for possible optical counterparts of radio bursts, time of arrivals of single optical (320–900 nm) photons were rebinned at 1 ms resolution and computing our ULs with

this resolution to be consistent with the results obtained by Asiago.

We searched for the optical counterpart in two different time intervals (±15 s and ±100 ms) around the epoch of the detection of all the seven bursts detected by uGMRT. Since no significant peaks were found at the time of bursts, we placed only an upper limit on the magnitude. This value was computed for each burst by adopting the same procedure as that reported in Sect. 3.2.1. Following the SiFAP2 calibration curve[3], we obtained a non-dereddened UL magnitude of $V = 15.96$, and $V = 16.42$, for the ±15 s and ±100 ms time intervals, respectively. The corresponding fluence densities are 1.56 mJy ms and 1.02 mJy ms.

3.3. High-energy observations

3.3.1. AGILE

We searched in archival Super-A, MCAL, and GRID data, at the times reported in Table 2, to look for coincident X-ray and γ-ray emission from the source. As we reported in Table A.3, AGILE has partial coverage of the 21 bursts reported. Of the 12 bursts in the MCAL FoV, we found no evidence of significant signals in the data. We were able to provide standard MCAL fluence ULs at 3σ when a data interval is present and sub-ms fluence ULs when no data acquisition is available. Moreover, due to the AGILE spinning and to the reduced Super-A and GRID FoV with respect to the MCAL FoV, only one event falls inside the GRID exposed region and none in the Super-A one. However this burst falls within a data acquisition gap and hence we cannot provide a punctual UL. We could provide also GRID 3σ ULs in $E \geq 100$ MeV on two integrations: over 6 days, obtaining $\mathrm{UL}_{6\mathrm{days}} = 6.0 \times 10^{-11}$ erg cm^{-2} s^{-1}, and on about 17 months from 2020/04/01 to 2021/09/15, with $\mathrm{UL}_{17\mathrm{months}} = 7.7 \times 10^{-12}$ erg cm^{-2} s^{-1}.

3.3.2. Insight–HXMT

We carried out two kinds of searches: (i) a blind one conducted irrespective of the radio bursts, by applying the criteria that have already been tailored and applied to *Insight*–HXMT data in previous investigations (Guidorzi et al. 2020); (ii) a targeted search around the times of the FRBs that were covered with *Insight*–HXMT observations. The expected background counts were estimated following the prescriptions of Guidorzi et al. (2020). We did not find any statistically significant ($>3\sigma$ confidence) candidate in either case. Hereafter, we focus on the results of (ii), whereas a more detailed report on the results of (i) will be reported elsewhere.

We simultaneously observed 7 out of the 21 FRBs reported in this work (Table 2) with *Insight*–HXMT. In particular, we covered simultaneously with both LE and ME 5 FRBs detected with the SRT (SRT-P-01, SRT-P-02, SRT-P-07, SRT-P-08, and SRT-P-09), whereas uGMRT-01 was covered with all of the three *Insight*–HXMT instruments and uGMRT-02 with the ME only. For each of these 7 FRBs, we carried out a search for statistically significant excesses within a time window centred on the FRB time with a duration of 200 s or shorter, depending on the availability of data. To account for the unknown duration of any possible high-energy counterpart, we spanned a logarithmically-spaced range of bin times, from 1, 2, 4,…to 128 ms. In each case, we applied a threshold on the counts of each individual detector as well as to the summed counts by imposing a

---

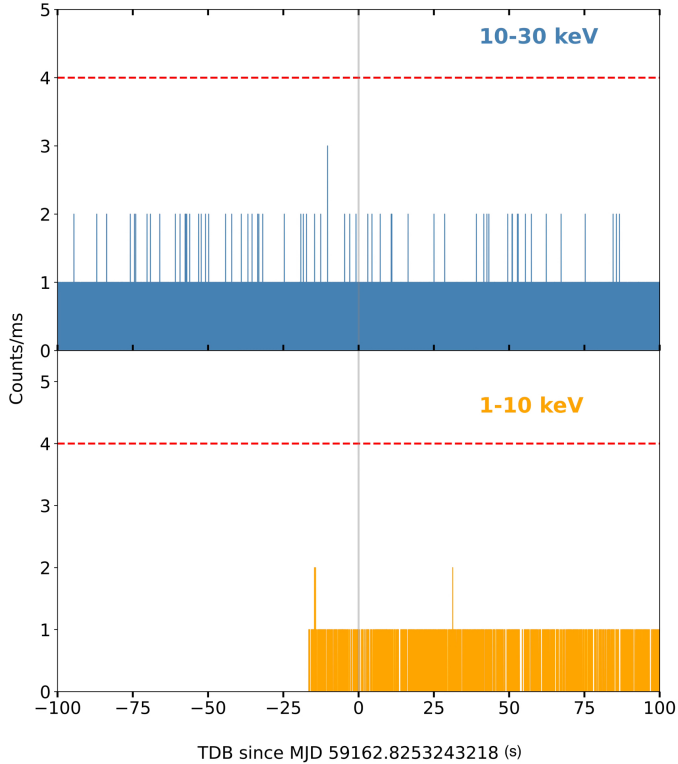[3] https://www.tng.iac.es/instruments/sifap2/

Fig. 8. *Insight*–HXMT 1-ms light curves of LE and ME obtained around SRT-P-01 (grey line). Dashed lines show the $\approx 3\sigma$ upper limits that account for the multi-trial search.

detection significance of $p_{\mathrm{sing}}/N_{\mathrm{bins}}$, with p_{sing} as close as possible to 2.7×10^{-3} (i.e. 3σ confidence), taking into account the multitrial due to the number of bins N_{bins} to be screened. Since the expected background counts in each instrument are $\ll 1$ over a few ms and because of the discreteness of Poisson distribution, the probability associated with a given threshold on the number of counts varies enormously even by changing the threshold by one: this is why the corresponding significance can only approximately be 3σ for most cases.

We did not find any counts in excess of the thresholds. We therefore calculated the threshold counts on the summed light curves (LE+ME for the 5 SRT FRBs, LE+ME+HE for uGMRT-01, and ME only for uGMRT-02) for three representative bin times (1, 16, and 128 ms). We then converted these ULs on counts to corresponding fluence values by considering three different spectral models that were discussed by Guidorzi et al. (2020) and that can be plausibly expected for sources like magnetars: a power-law (PL) with photon index $\Gamma = 2$, an optically thin thermal bremsstrahlung (OTTB) with either $kT = 50\,\mathrm{keV}$ or $kT = 200\,\mathrm{keV}$.

Table A.8 reports the corresponding fluence limits in either $1-30$, or $1-100$, or $10-30\,\mathrm{keV}$ energy passbands, depending on whether data from: LE and ME only were available, from all of the three instruments, or from the ME only, respectively. Overall, for each of the three integration times mentioned above, the corresponding $\approx 3\sigma$ ULs on the $1-30\,\mathrm{keV}$ fluence are in the range $(1.6-2.9) \times 10^{-10}\,\mathrm{erg\,cm^{-2}}$ (1 ms), $(2.7-5.5) \times 10^{-10}\,\mathrm{erg\,cm^{-2}}$ (16 ms), and $(5.5-12) \times 10^{-10}\,\mathrm{erg\,cm^{-2}}$ (128 ms). Figure 8 shows the *Insight*–HXMT coverage with 1 ms resolution of SRT-P-01 with LE and ME, along with the corresponding $\approx 3\sigma$ detection threshold.

3.3.3. INTEGRAL

In the complete integrated mosaics of the INTEGRAL Soft Gamma-ray Imager (ISGRI) and the Joint European X-ray Monitor (JEM-X), we did not detect bursts from R3 and we use ISGRI observations to set an UL of $1.1 \times 10^{-11}\,\mathrm{erg\,cm^{-2}\,s^{-1}}$ on an average source flux in 28–80 keV band assuming a power-law spectrum with a slope of 2. The limit on average source flux with JEM-X can be set in 3–30 keV band at the level $3.6 \times 10^{-11}\,\mathrm{erg\,cm^{-2}\,s^{-1}}$.

In order to search for possible variable emission, we built ISGRI light curves on timescales of 1000 s and s, in 28–80 keV energy range. We do not detect any variable emission on these timescales and put ULs of $2.7 \times 10^{-10}\,\mathrm{erg\,cm^{-2}\,s^{-1}}$ and $1.1 \times 10^{-8}\,\mathrm{erg\,cm^{-2}\,s^{-1}}$ on 1000 s and 1 s long impulsive emission.

Unfortunately, none of the bursts occurred when R3 was in the FoV of INTEGRAL pointing instruments. However, INTEGRAL all-sky instruments were taking data during all of the radio events and we derive an UL on 1-second long hard X-ray burst within 10 s from each radio burst, as shown in Table A.6.

3.3.4. *Swift*

We carried out a search for the presence of an X-ray source candidate at the R3 position in the whole *Swift*/XRT WT mode dataset. No X-ray source was detected (a $>3\sigma$ confidence was required). We therefore extracted the 3σ countrate ULs using the XIMAGE package (sosta command) and converted to fluxes using a standard single power-law spectral model with a photon index of 2.0, and correcting for absorption for a column density N_{H} fixed to the Galactic value of $7.1 \times 10^{21}\,\mathrm{cm^{-2}}$ (HI4PI Collaboration 2016) redshifted for the known $z = 0.0337$ (Marcote et al. 2020). The X-ray observations exposure and the corresponding ULs are reported in Table A.7.

4. Discussion

Figure 9 shows an overview of the isotropic luminosity ULs by all the instruments involved in this MWL campaign. We can use these punctual ULs to constrain the optical/radio and high-energy/radio energy ratios. SRT-P-02 was observed simultaneously with Aqueye+ and CMO SAI MSU. Assuming that the burst width is of the same order of tens of ms in both bands, this implies a ratio $\xi = E_{\mathrm{optical}}/E_{\mathrm{radio}} < 7.8 \times 10^2$ and $\xi < 5.6 \times 10^2$, respectively. CMO SAI MSU UL however, is obtained from a camera (iXon 897) while Asiago uses a fast photometer (Aqueye+) and the observations are performed and reduced via different techniques. In the case of the search for an optical counterpart of a signal like an FRB, due to its short duration, a fast photometer is more capable to explore such low duration ranges. The radio burst uGMRT-03 was simultaneous with Aqueye+ and SiFAP2 observations and, with their punctual UL, we can constrain the ratio $\xi < 6.9 \times 10^2$ for Aqueye+ and $\xi < 1.3 \times 10^2$ for SiFAP2. SiFAP2 UL on R3 is the most stringent UL on the optical emission for this source to date. The prior most stringent UL in the optical band for R3 was from Andreoni et al. (2020). They performed untargeted observations of R3, not simultaneous with a radio instrument, with the Zwicky Transient Facility, monitoring the source in active windows and providing an UL of $\xi < 10^8$.

Beloborodov (2020) describes a scenario where young, hyperactive magnetars are the progenitors of FRBs. Their magnetic flares are able to generate blast waves in the surrounding wind medium and this could result into optical flashes, of the

duration of up to ~1 s, simultaneous to the radio bursts. Given their formation, in the tail of a preceding flare, they are expected during recurrent flaring episodes, and they are expected to be weak unless they are formed after a strong explosion, when they could reach $E_{\text{optical}} \sim 10^{44}$ erg. Only our current UL, for both dates when more bursts were observed, can exclude such strong flares at the moment.

SRT-P-02 was also simultaneous with *Insight*–HXMT observations, which provided a punctual UL (1–30 keV band) on the released isotropic energy $E_{\text{X−ray}}$, in the range of $(2−3) \times 10^{45}$ erg for a time bin of 128 ms, depending on which emission model is considered (see Sect. 3.3.2). This UL is of the same order of magnitude of the ones placed by *Chandra* (Scholz et al. 2020) and *XMM-Newton* (Pilia et al. 2020) for the same source also simultaneously with a radio burst. In the case of the SRT-P-02 burst, this UL implies an UL in the X-ray/radio efficiency $\eta = E_{\text{X}}/E_{\text{radio}} < (0.9−1.3) \times 10^7$.

It is worthwhile making a comparison with the case of the SGR J1935+2154 event. With its bi-chromatic simultaneous detection in radio (CHIME/FRB Collaboration 2020; Bochenek et al. 2020) and at high energies (Mereghetti et al. 2020; Tavani et al. 2021; Zhang et al. 2020b; Ridnaia et al. 2021), it provided evidence that magnetars can be FRB emitters and, hence, act as the sources behind at least some of the FRBs observed. In that case, the energy released for the burst detected by CHIME was ~3×10^{34} erg and it corresponded, in the 1–250 keV band of *Insight*–HXMT, to ~1×10^{39} erg (Zhang et al. 2020b), implying $\eta \sim 10^5$. This value is two orders of magnitude smaller than the η UL that we reached with our MWL observations for R3. With this current UL we cannot exclude X-ray/radio efficiencies η ten times greater or of the same order of magnitude of the efficiency of the SGR J1935+2154 event.

If we compare the results of our multi-cycle MWL campaign on R3 to the evidence based on the single event associated to the SGR J1935+2154 burst, we conclude that the detection of a R3 radio burst with fluence $\gtrsim 10^3$ Jy ms would allow us to set constraints on η matching those of the Galactic event, in light of the sensitivity thresholds of current X-ray telescopes. If we determine the threshold of a given X-ray instrument as $F^*_{\text{X−ray}}$, we can express the corresponding radio fluence density F_ν, with the assumption of an efficiency η as:

$$F_\nu = \frac{F^*_{\text{X−ray}}}{\eta \Delta \nu}, \tag{2}$$

where $\Delta\nu$ is the frequency width of the radio burst. We assume the average value of $\Delta\nu = 107 \pm 59$ MHz, as discussed in Sect. 3.1. We can now compute via Eq. (1) the rate of events $R(>F_\nu)$ with a radio fluence density greater than F_ν for the SRT-P and uGMRT Band 3. By performing the same Monte Carlo simulation for uGMRT Band 3 (as discussed in Sect. 3.1.3), we obtained a value of $\zeta(200 \text{ MHz}, 0.6 \text{ Jy ms}) = 0.43 \pm 0.04$. Adopting the assumption that the R3 bursting activity is Poissonian, using the expected rate $R(>F_\nu)$, we can roughly estimate the detection probability, $p(>F_\nu)$, of detecting one or more bursts with fluence density $>F_\nu$ in a campaign of duration ΔT:

$$p(>F_\nu) = 1 - e^{-R(>F_\nu)\Delta T}. \tag{3}$$

Figure 10 shows the probability computed via Eq. (3) for an X-ray detection simultaneous with the SRT-P or the uGMRT Band 3 as a function of the time of simultaneous exposure. Evaluating how sensitive a certain X-ray satellite may be to a putative X-ray burst requires several assumptions to be made on the emission mechanism of the source in order to get a punctual
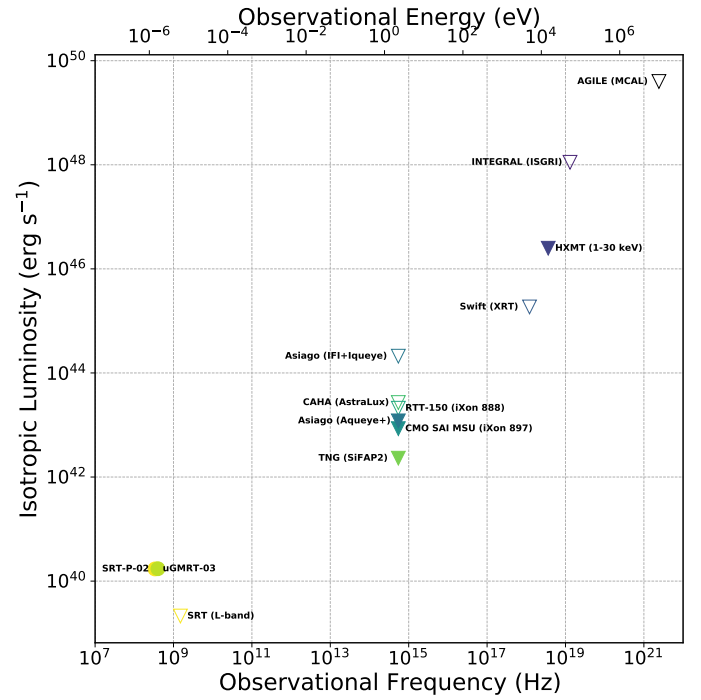

Fig. 9. Burst isotropic luminosity as function of the observational frequency for all the instruments involved in the MWL campaign. The dots are the luminosities of the bursts SRT-P-02 and uGMRT-03. The empty triangle markers represent the non punctual upper limits (ULs), that is coincident with no radio bursts. The filled triangles are punctual ULs, coincident with a radio burst detection (see Sect. 4). All optical ULs are converted in the *V* band and for a 1 ms burst.

value for $F^*_{\text{X−ray}}$. Keeping the discussion to the level of orders of magnitude, the X-ray telescopes involved in the campaign were capable to detect bursts with a fluence threshold in the range of $10^{-10}–10^{-7}$ erg cm^{-2}. Considering a 99.9% detection probability, this would require X-ray/radio campaigns that would be $3 \times 10^2–3 \times 10^6$ h long for $\eta = 10^6$, or $6 \times 10^3–5 \times 10^7$ h for $\eta = 10^5$, with respect to the X-ray thresholds considered.

5. Summary and conclusions

This work presents the results of a multi-wavelength observational campaign on FRB 20180916B (R3) performed between October 2020 and August 2021. The campaign involved the SRT and the uGMRT radio telescopes, the *Galileo* and *Copernico* (Asiago), CMO SAI MSU, CAHA 2.2m, and RTT-150 optical telescopes, and, lastly, the high-energy satellites AGILE, *Insight*–HXMT, INTEGRAL, and *Swift*.

We detected 14 new bursts with the SRT at 336 MHz and 7 new bursts with the uGMRT at 400 MHz. Neither the optical instruments nor the high-energy ones detected statically significant bursts at their frequencies. Asiago reports an optical peak within a window of ±15 s around the second radio burst detected by the SRT on the night of 2020/11/09. The peak is above the threshold of the aforementioned window of 30 s of 15 counts bin^{-1}. However, it is slightly below the 19-count bin^{-1} threshold obtained considering the statistics of the entire observation, so it is not possible to robustly tag it as the optical counterpart of the radio burst.

We constrained the optical/radio efficiency ξ setting a punctual upper limit (UL) thanks to a radio detection with the uGMRT and a simultaneous observation with the SiFAP2
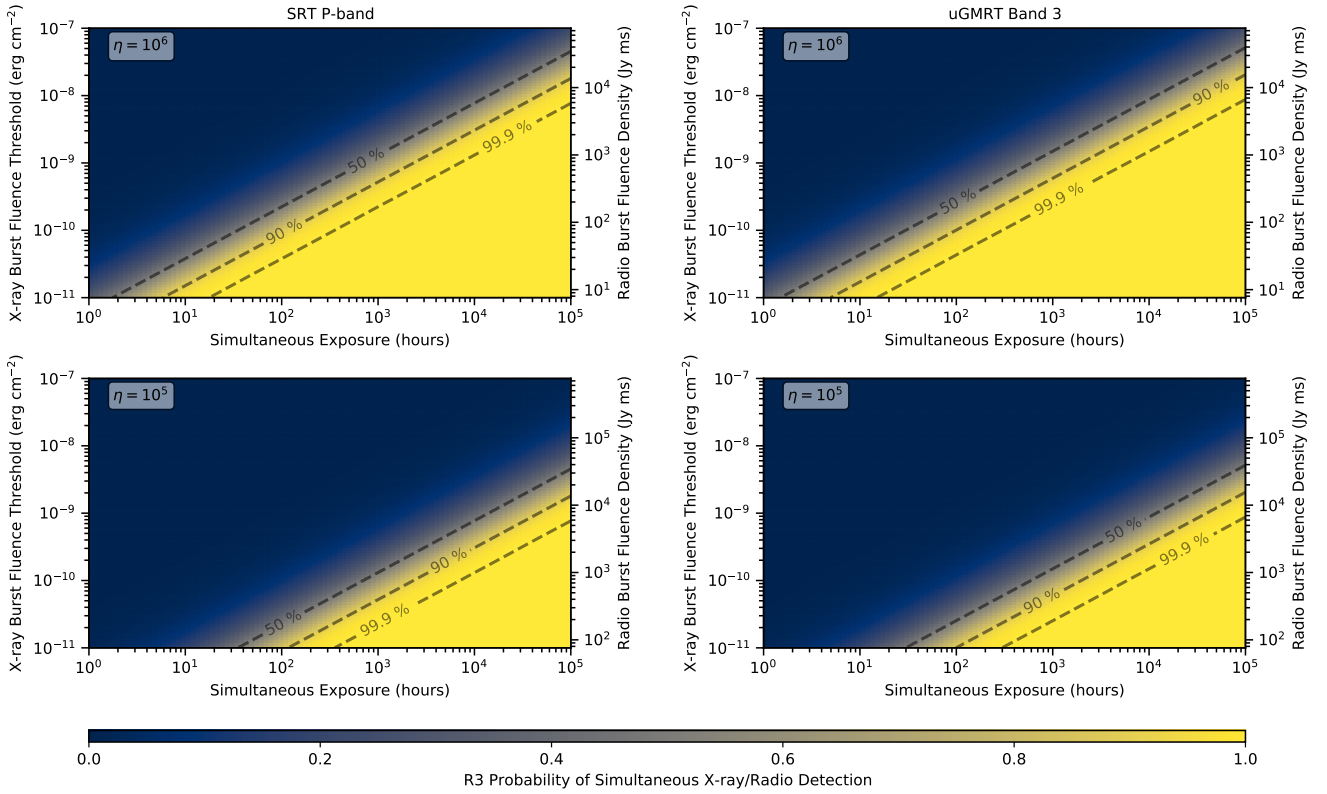
Fig. 10. Probability of detecting a X-ray/radio event given a certain X-ray/radio efficiency η observing in the radio band with the SRT-P (left) or the uGMRT Band 3 (right). Supposing that the event is above the fluence X-ray threshold (left y-axis) the colormap shows the probability of detecting a radio burst with radio fluence (right y-axis), constrained by the efficiency η, as a function of the simultaneous exposure (x-axis). The dashed lines represent the iso-probability contour plots for a probability of 50, 90, and 99.9 %.

photometer installed at the TNG. We set a constraint of $\xi < 1.3 \times 10^2$, thereby reporting the deepest UL in the optical band for this source.

The *Insight*–HXMT observations, occurring simultaneously with a radio burst detected by the SRT, set a punctual UL on the X-ray-and-radio efficiency η in the range of $\eta < (0.9 - 1.3) \times 10^7$ (1–30 keV band), depending on which emission model is used for the X-ray emission. Assuming the efficiency η is either 10^6 or 10^5 (with the latter being comparable to that of the SGR J1935+2154 event), we can estimate what the required simultaneous X-ray-and-radio observing time and X-ray burst fluence should be to reach a given detection probability, with the instrumentation available in our campaign. Assuming that the events follow a Poissonian statistics, for X-ray sensitivities in the range of $10^{-10} - 10^{-7}$ erg cm^{-2}, simultaneous X-ray/radio campaigns should last between $3 \times 10^2 - 3 \times 10^6$ h for $\eta = 10^6$ or $6 \times 10^3 - 5 \times 10^7$ h for $\eta = 10^5$. This result poses challenges in terms of the detectability of a putative X-ray burst from this source. This can mainly be attributed to the cosmological nature of R3, being distant about 150 Mpc, which is ~10^4 times farther than the only source which has emitted an FRB-like signal simultaneous with an X-ray burst to date: SGR J1935+2154. Despite the existence of closer-by repeaters (e.g., FRB 20200120E, Kirsten et al. 2022; FRB 20181030A, Bhardwaj et al. 2021), R3 represents at present a golden source for a MWL follow-up for its periodic activity, high repetition rate, and the relatively high energetic nature of the bursts.

References

Aggarwal, K. 2021, ApJ, 920, L18
Aggarwal, K., Agarwal, D., Kania, J. W., et al. 2020, J. Open Source Software, 5, 2750

Ambrosino, F., Cretaro, P., Meddi, F., et al. 2016, J. Astron. Instrum., 5, 1650005
Andreoni, I., Lu, W., Smith, R. M., et al. 2020, ApJ, 896, L2
Barbieri, C., Naletto, G., Occhipinti, T., et al. 2009, J. Mod. Opt., 56, 261
Barsdell, B. R., Bailes, M., Barnes, D. G., & Fluke, C. J. 2012, MNRAS, 422, 379
Bassa, C. G., Janssen, G. H., Karuppusamy, R., et al. 2016, MNRAS, 456, 2196
Beloborodov, A. M. 2017, ApJ, 843, L26
Beloborodov, A. M. 2020, ApJ, 896, 142
Bethapudi, S., Spitler, L. G., Main, R. A., Li, D. Z., & Wharton, R. S. 2022, MNRAS, submitted [arXiv:2207.13669]
Bhardwaj, M., Kirichenko, A. Y., Michilli, D., et al. 2021, ApJ, 919, L24
Bochenek, C. D., Ravi, V., Belov, K. V., et al. 2020, Nature, 587, 59
Bulgarelli, A., Chen, A. W., Tavani, M., et al. 2012, A&A, 540, A79
Burrows, D. N., Hill, J. E., Nousek, J. A., et al. 2005, Space Sci. Rev., 120, 165
Caleb, M., Stappers, B. W., Abbott, T. D., et al. 2020, MNRAS, 496, 4565
Cao, X., Jiang, W., Meng, B., et al. 2020, Sci. China Phys. Mech. Astron., 63, 249504
Casentini, C., Verrecchia, F., Tavani, M., et al. 2020, ApJ, 890, L32
Chamma, M. A., Rajabi, F., Wyenberg, C. M., Mathews, A., & Houde, M. 2021, MNRAS, 507, 246
Chatterjee, S., Law, C. J., Wharton, R. S., et al. 2017, Nature, 541, 58
Chawla, P., Andersen, B. C., Bhardwaj, M., et al. 2020, ApJ, 896, L41
Chen, Y., Cui, W., Li, W., et al. 2020, Sci. China Phys. Mech. Astron., 63, 249505
CHIME/FRB Collaboration (Andersen, B. C., et al. 2019a, ApJ, 885, L24
CHIME/FRB Collaboration (Andersen, B. C., et al.) 2019b, ApJ, 885, L24
CHIME/FRB Collaboration (Amiri, M., et al.) 2020, Nature, 582, 351
CHIME/FRB Collaboration (Amiri, M., et al.) 2020, Nature, 587, 54
Cruces, M., Spitler, L. G., Scholz, P., et al. 2021, MNRAS, 500, 448
Feroci, M., Costa, E., Soffitta, P., et al. 2007, Nucl. Instrum. Methods Phys. Res. A, 581, 728
Ghedina, A., Leone, F., Ambrosino, F., et al. 2018, SPIE Conf. Ser., 10702, 107025Q
Ghisellini, G., & Locatelli, N. 2018, A&A, 613, A61
Guidorzi, C., Orlandini, M., Frontera, F., et al. 2020, A&A, 642, A160
Gupta, Y., Ajithkumar, B., Kale, H. S., et al. 2017, Curr. Sci., 113, 707
Hardy, L. K., Dhillon, V. S., Spitler, L. G., et al. 2017, MNRAS, 472, 2800
Hessels, J. W. T., Spitler, L. G., Seymour, A. D., et al. 2019, ApJ, 876, L23
Hewitt, D. M., Snelders, M. P., Hessels, J. W. T., et al. 2022, MNRAS, 515, 3577
HI4PI Collaboration (Ben Bekhti, N., et al.) 2016, A&A, 594, A116
Hobbs, G. B., Edwards, R. T., & Manchester, R. N. 2006, MNRAS, 369, 655
Hormuth, F., Hippler, S., Brandner, W., Wagner, K., & Henning, T. 2008, SPIE Conf. Ser., 7014, 701448
Hotan, A. W., van Straten, W., & Manchester, R. N. 2004, PASA, 21, 302
Jahns, J. N., Spitler, L. G., Nimmo, K., et al. 2023, MNRAS, 519, 666
Kirsten, F., Marcote, B., Nimmo, K., et al. 2022, Nature, 602, 585
Kumar, P., Lu, W., & Bhattacharya, M. 2017, MNRAS, 468, 2726
Kumar, P., Shannon, R. M., Flynn, C., et al. 2021, MNRAS, 500, 2525
Law, C. J., Abruzzo, M. W., Bassa, C. G., et al. 2017, ApJ, 850, 76
Li, D., Wang, P., Zhu, W. W., et al. 2021, Nature, 598, 267
Liu, C., Zhang, Y., Li, X., et al. 2020, Sci. China Phys. Mech. Astron., 63, 249503
Lorimer, D. R. 2011, Astrophysics Source Code Library [record ascl:1107.016]
Lorimer, D., & Kramer, M. 2005, Handbook of Pulsar Astronomy, Cambridge Observing Handbooks for Research Astronomers (Cambridge University Press)
Lyubarsky, Y. 2014, MNRAS, 442, L9
Lyutikov, M., Barkov, M. V., & Giannios, D. 2020, ApJ, 893, L39
Macquart, J. P., Shannon, R. M., Bannister, K. W., et al. 2019, ApJ, 872, L19
Majid, W. A., Pearlman, A. B., Nimmo, K., et al. 2020, ApJ, 897, L4
Marcote, B., Paragi, Z., Hessels, J. W. T., et al. 2017, ApJ, 834, L8
Marcote, B., Nimmo, K., Hessels, J. W. T., et al. 2020, Nature, 577, 190
Margalit, B., Beniamini, P., Sridhar, N., & Metzger, B. D. 2020, ApJ, 899, L27
Mckinven, R., Gaensler, B. M., Michilli, D., et al. 2023, ApJ, 950, 12
Mereghetti, S., Savchenko, V., Gotz, D., et al. 2020, GRB Coordinates Network, 27668, 1
Metzger, B. D., Margalit, B., & Sironi, L. 2019, MNRAS, 485, 4091
Naletto, G., Barbieri, C., Occhipinti, T., et al. 2009, A&A, 508, 531
Nita, G. M., & Hellbourg, G. 2020, in XXXIIIrd General Assembly and Scientific Symposium of the International Union of Radio Science, 1
Pastor-Marazuela, I., Connor, L., van Leeuwen, J., et al. 2021, Nature, 596, 505
Pearlman, A. B., Majid, W. A., Prince, T. A., et al. 2020, ApJ, 905, L27
Perley, R. A., & Butler, B. J. 2017, ApJS, 230, 7
Petroff, E., Bailes, M., Barr, E. D., et al. 2015, MNRAS, 447, 246
Petroff, E., Hessels, J. W. T., & Lorimer, D. R. 2022, A&ARv, 30, 2

Pilia, M., Burgay, M., Possenti, A., et al. 2020, ApJ, 896, L40
Pleunis, Z., Michilli, D., Bassa, C. G., et al. 2021, ApJ, 911, L3
Rajwade, K. M., Mickaliger, M. B., Stappers, B. W., et al. 2020, MNRAS, 495, 3551
Reddy, S. H., Kudale, S., Gokhale, U., et al. 2017, J. Astron. Instrum., 6, 1641011
Ridnaia, A., Svinkin, D., Frederiks, D., et al. 2021, Nat. Astron., 5, 372
Sand, K. R., Faber, J. T., Gajjar, V., et al. 2022, ApJ, 932, 98
Scholz, F. W., & Stephens, M. A. 1987, J. Am. Stat. Assoc., 82, 918
Scholz, P., Spitler, L. G., Hessels, J. W. T., et al. 2016, ApJ, 833, 177
Scholz, P., Bogdanov, S., Hessels, J. W. T., et al. 2017, ApJ, 846, 80
Scholz, P., Cook, A., Cruces, M., et al. 2020, ApJ, 901, 165
Shatsky, N., Belinski, A., Dodin, A., et al. 2020, in Ground-Based Astronomy in Russia. 21st Century, eds. I. I. Romanyuk, I. A. Yakunin, A. F. Valeev, & D. O. Kudryavtsev, 127
Spitler, L. G., Cordes, J. M., Hessels, J. W. T., et al. 2014, ApJ, 790, 101
Spitler, L. G., Scholz, P., Hessels, J. W. T., et al. 2016, Nature, 531, 202
Swarup, G., Ananthakrishnan, S., Kapahi, V. K., et al. 1991, Curr. Sci., 60, 95
Tavani, M. 2019, Rendiconti Lincei. Scienze Fisiche e Naturali, 14
Tavani, M., Barbiellini, G., Argan, A., et al. 2009, A&A, 502, 995
Tavani, M., Verrecchia, F., Casentini, C., et al. 2020, ApJ, 893, L42
Tavani, M., Casentini, C., Ursi, A., et al. 2021, Nat. Astron., 5, 401
Trudu, M., Pilia, M., Bernardi, G., et al. 2022, MNRAS, 513, 1858
Tuo, Y., Li, X., Ge, M., et al. 2022, ApJS, 259, 14
Ursi, A., Verrecchia, F., Piano, G., et al. 2022, ApJ, 924, 80
Valente, G., Pisanu, T., Bolli, P., et al. 2010, SPIE Conf. Ser., 7741, 774126
van Straten, W., & Bailes, M. 2011, PASA, 28, 1
Verrecchia, F., Casentini, C., Tavani, M., et al. 2021, ApJ, 915, 102
Zampieri, L., Naletto, G., Barbieri, C., et al. 2015, SPIE Conf. Ser., 9504, 95040C
Zampieri, L., Naletto, G., Barbieri, C., et al. 2016, SPIE Conf. Ser., 9907, 99070N
Zampieri, L., Naletto, G., Barbieri, C., et al. 2019, Contrib. Astron. Obs. Skalnate Pleso, 49, 85
Zampieri, L., Mereghetti, S., Turolla, R., et al. 2022, ApJ, 925, L16
Zhang, B. 2022, arXiv e-prints [arXiv:2212.03972]
Zhang, S. N., Tuo, Y. L., Xiong, S. L., et al. 2020a, ATel, 13687, 1
Zhang, S.-N., Li, T., Lu, F., et al. 2020b, Sci. China Phys. Mech. Astron., 63, 249502
Zhang, Y. G., Gajjar, V., Foster, G., et al. 2018, ApJ, 866, 149

[1] Università degli Studi di Cagliari, Dipartimento di Fisica, SP Monserrato-Sestu km 0.7, 09042 Monserrato (CA), Italy
e-mail: matteo.trudu@inaf.it
[2] INAF-Osservatorio Astronomico di Cagliari, via della Scienza 5, 09047 Selargius (CA), Italy
[3] INAF – Osservatorio di Astrofisica e Scienza dello Spazio di Bologna, Via Piero Gobetti 93/3, 40129 Bologna, Italy
[4] Department of Physics and Earth Science, University of Ferrara, via Saragat 1, 44122 Ferrara, Italy
[5] INFN – Sezione di Ferrara, via Saragat 1, 44122 Ferrara, Italy
[6] INAF – Osservatorio Astronomico di Padova, Vicolo dell'Osservatorio 5, 35122 Padova, Italy
[7] National Centre for Radio Astrophysics, Tata Institute of Fundamental Research, Post Bag 3, Ganeshkhind, Pune 411 007, India
[8] INAF/IAPS, via del Fosso del Cavaliere 100, 00133 Roma (RM), Italy
[9] Sapienza Università di Roma, Piazzale Aldo Moro 5, 00185 Roma (RM), Italy
[10] INFN Sezione di Roma 2, via della Ricerca Scientifica 1, 00133 Roma (RM), Italy
[11] Space Research Institute, Russian Academy of Sciences, Profsoyuznaya 84/32, 117997 Moscow, Russia
[12] ISDC, Department of Astronomy, University of Geneva, Chemin d'Ecogia, 16 CH-1290 Versoix, Switzerland
[13] SSDC/ASI, via del Politecnico snc, 00133 Roma (RM), Italy
[14] INAF – Osservatorio Astrofisico di Roma, via Frascati 33, 00078 Monte Porzio Catone (RM), Italy
[15] INAF-Istituto di Radio Astronomia, via Gobetti 101, 40129 Bologna, Italy
[16] Department of Physics and Electronics, Rhodes University, PO Box 94, Grahamstown 6140, South Africa
[17] South African Radio Astronomy Observatory, Black River Park, 2 Fir Street, Observatory, Cape Town 7925, South Africa

[18] INAF – Osservatorio Astrofisico di Arcetri, Largo Enrico Fermi 5, 50125 Florence, Italy

[19] Department of Physics and Astronomy, University of Padova, Via F. Marzolo 8, 35131 Padova, Italy

[20] Department of Astronomy, University of California Berkeley, Berkeley, CA 94720, USA

[21] Instituto de Astrofísica de Andalucía, Glorieta de la Astronomía s/n, 18008 Granada, Spain

[22] CAHA – Centro Astronómico Hispano en Andalucía, Observatorio de Calar Alto, Sierra de los Filabres, 04550 Gérgal, Almería, Spain

[23] Key Laboratory of Particle Astrophysics, Institute of High Energy Physics, Chinese Academy of Sciences, 19B Yuquan Road, Beijing 100049, PR China

[24] Fundación Galileo Galilei – INAF, Rambla J.A. Fernández P. 7, 38712 S.C.Tenerife, Spain

[25] Sternberg Astronomical Institute, Moscow M.V. Lomonosov State University, Universitetskij pr., 13, 119992 Moscow, Russia

[26] Università degli Studi di Roma "Tor Vergata", via della Ricerca Scientifica 1, 00133 Roma (RM), Italy

[27] University of Chinese Academy of Sciences, Chinese Academy of Sciences, Beijing 100049, PR China

Appendix A: Additional instrumental material: Observation logs and upper limits

Table A.1. Log of the optical observations of R3 carried out with Aqueye+ at *Copernicus* and IFI+Iqueye at *Galileo*.

Camera (telescope)	Observation ID	Start Time (topocentric) [UTC]	Exposure [s]
Aqueye+ (*Copernicus*)	20201025-033103_gti1	2020-10-25 03:01:54.000	1748
	20201025-045249_gti1	2020-10-25 03:52:51.000	520
	20201109-200635	**2020-11-09 19:06:36.000**	**7198**
	20201109-221239_gti1	2020-11-09 21:26:00.000	2797
	20201109-231359	**2020-11-09 22:14:00.000**	**8997**
	20201110-020901	2020-11-10 01:09:02.000	1797
	20201110-024652	2020-11-10 01:46:53.000	897
	20201110-192232_gti1	2020-11-10 19:28:24.000	6848
	20201110-224746	2020-11-10 21:47:47.000	10798
	20201111-014901	2020-11-11 00:49:03.000	1798
	20201111-023825	2020-11-11 01:38:26.000	1198
	20201111-231309_gti1	2020-11-11 22:32:20.000	2050
	20201112-005752_gti1	2020-11-11 23:59:23.000	3508
	20201112-015938	2020-11-12 00:59:40.000	3598
	20201112-193512	2020-11-12 18:35:14.000	3598
	20201112-205147	2020-11-12 19:51:48.000	3597
	20201113-214903	2020-11-13 20:49:04.000	3597
	20210111-193142	2021-01-11 18:31:44.000	7981
	20210111-220228_gti1	2021-01-11 21:02:29.000	1950
	20210112-190452	2021-01-12 18:04:53.000	7197
	20210112-210529	2021-01-12 20:05:31.000	7198
	20210113-190245_gti1	2021-01-13 18:02:46.000	850
	20210113-210411_gti1	2021-01-13 20:04:13.000	1650
	20210113-210411_gti2	2021-01-13 20:34:13.000	2300
	20210114-183758_gti1	2021-01-14 17:43:49.000	5300
	20210813-232725	2021-08-13 21:27:26.000	7197
	20210814-012913	2021-08-13 23:29:14.000	7197
	20210814-234903	2021-08-14 21:49:04.000	7197
	20210815-014951	**2021-08-14 23:49:53.000**	**7198**
	20210815-035032	2021-08-15 01:50:34.000	898
	20210815-040612	2021-08-15 02:06:14.000	898
IFI+Iqueye (*Galileo*)	**20201109-211141**	**59162 20:11:43.0**	**7197**
	20201109-233529_gti1	**59162 22:35:31.0**	**6850**
	20201110-013640	59163 00:36:42.0	2697
	20201110-193505_gti1	59163 18:35:07.0	7700
	20201110-223616	59163 21:36:19.0	1797
	20201110-233217	59163 22:32:19.0	3597
	20210213-195451	**59258 18:54:53.0**	**5398**
	20210213-212539_gti1	59258 20:47:21.0	2897
	20210214-192834	59259 18:28:37.0	7197
	20210214-212932	59259 20:29:34.0	4197
	20210215-191649	59260 18:16:51.0	7197
	20210215-211741	59260 20:17:44.0	5397

Notes. Observations in bold are the ones in which a radio burst has been detected.

Table A.2. Observation log of CMO SAI MSU, RTT-150, CAHA 2.2m, and TNG.

Camera telescope)	Start time (topocentric)	Exposure [ks]
iXon 897 (CMO SAI MSU)	2020-11-09 17:31:00.0	3.84
	2020-11-09 19:18:00.0	29.28
	2020-11-10 17:42:00.0	24.48
iXon 888 (RTT-150)	2020-11-10 10:00:00.0	27.00
AstraLux (CAHA 2.2m)	2021-01-13 19:24:25.0	3.60
	2021-01-13 20:36:01.0	3.60
	2021-01-13 21:47:36.0	3.60
	2021-01-13 22:59:19.0	1.08
SiFAP2 (TNG)	2021-08-15 00:35:00.0	8.7

Table A.3. *AGILE* Coverage and MCAL upper limits (ULs) during the R3 radio bursts.

Burst ID	MCAL FoV	MCAL D.A.	GRID FoV	UL (3σ) [erg cm^{-2}]	UL (sub-ms) [erg cm^{-2}]
SRT-P-01	NO	NO	NO	earth occultation	
SRT-P-02	NO	NO	NO	earth occultation	
SRT-P-03	YES	NO	NO	—	1.15×10^{-8}
SRT-P-04	YES	NO	YES	—	2.55×10^{-8}
SRT-P-05	YES	NO	NO	—	6.88×10^{-8}
SRT-P-06	NO	NO	NO	earth occultation	
SRT-P-07	NO	NO	NO	earth occultation	
SRT-P-08	NO	NO	NO	earth occultation	
SRT-P-09	YES	NO	NO	—	6.88×10^{-8}
SRT-P-10	YES	NO	NO	—	6.88×10^{-8}
SRT-P-11	YES	YES	NO	1.07×10^{-6}	1.03×10^{-7}
SRT-P-12	NO	NO	NO	idle mode	
SRT-P-13	YES	NO	NO	—	1.83×10^{-8}
SRT-P-14	YES	NO	NO	—	3.60×10^{-8}
uGMRT-01	YES	YES	NO	1.03×10^{-6}	1.00×10^{-7}
uGMRT-02	NO	NO	NO	earth occultation	
uGMRT-03	NO	NO	NO	earth occultation	
uGMRT-04	NO	NO	NO	idle mode	
uGMRT-05	NO	NO	NO	idle mode	
uGMRT-06	YES	YES	NO	1.09×10^{-7}	1.06×10^{-8}
uGMRT-07	YES	YES	NO	2.36×10^{-7}	2.29×10^{-8}

Notes. The second and fourth columns report the presence and absence of the source in the FoV of the onboard detector, respectively. The third column reports the presence and absence of MCAL data acquisition. ULs (3σ) are evaluated on existing MCAL data acquisitions at the burst times and correspond to a fluence of 3σ above the background; ULs (sub-ms) are evaluated on the basis of the data acquisition (if present); otherwise, they refer to the UL fluences which would be required to issue a trigger with the onboard sub-ms MCAL trigger logic timescale (see Ursi et al. 2022). In presence of MCAL data acquisition, we show UL intervals obtained applying the spatial response matrix corresponding to source direction at burst times.

Table A.4. *Insight*–HXMT observation log.

Obs ID	Start time (topocentric)	Stop time (topocentric)	LE exposure [ks]	ME exposure [ks]	HE exposure [ks]
P0303077001	2020-10-23 17:21:49	2020-10-24 01:29:27	11.1	12.7	7.9
P0303077002	2020-10-24 17:12:47	2020-10-25 01:19:58	11.7	12.3	7.9
P0303077003	2020-11-09 16:29:24	2020-11-10 00:36:49	14.1	11.6	4.4
P0303077004	2020-11-10 16:21:02	2020-11-11 00:29:44	14.9	12.1	6.9
P0303077005	2021-01-12 16:55:51	2021-01-13 01:12:32	11.2	12.3	10.3
P0303077007	2021-01-13 16:46:54	2021-01-14 00:53:14	11.0	12.3	11.0
P0403084001	2021-08-13 19:37:53	2021-08-15 02:10:55	53.5	45.5	31.9

Table A.5. INTEGRAL observation log.

Start time (topocentric)	Stop time (topocentric)	Pointing ID	Exposure [ks]
2020-12-18 21:42	2020-12-18 22:12	231000350010 – 231000380010	7.2
2020-12-19 00:23	2020-12-19 00:53	231000400010 – 231000400010	1.8
2020-12-19 01:27	2020-12-19 01:57	231000420010 – 231000540010	23.3
2020-12-21 08:39	2020-12-21 09:09	231100250010 – 231100280010	7.2
2020-12-21 11:38	2020-12-21 12:08	231100310010 – 231100540010	43.1
2020-12-24 05:56	2020-12-24 06:26	231200350010 – 231200380010	7.2
2020-12-24 08:36	2020-12-24 09:06	231200400010 – 231200440010	9.0
2020-12-27 08:13	2020-12-27 08:44	231300540010 – 231300560010	7.1
2020-12-27 10:52	2020-12-27 11:21	231300580010 – 231300780010	37.7
2020-12-28 06:29	2020-12-28 06:59	231300950010 – 231301010010	12.6
2020-12-30 13:29	2020-12-30 13:59	231400810010 – 231400820010	3.6
2020-12-30 15:23	2020-12-30 15:53	231400850010 – 231401040010	35.9
2021-01-01 02:33	2021-01-01 03:03	231500300010 – 231500360010	12.6
2021-01-03 20:01	2021-01-03 20:31	231600330010 – 231600360010	7.2
2021-01-03 22:42	2021-01-03 23:12	231600380010 – 231600520010	27.0
2021-01-05 19:28	2021-01-05 19:59	231700020010 – 231700060010	9.1
2021-01-12 06:55	2021-01-12 07:21	231900540010 – 231900740010	70.9
2021-01-13 03:48	2021-01-13 04:45	231900750010 – 231900800010	20.9
2021-01-15 00:01	2021-01-15 01:26	232000340010 – 232000580010	88.4
2021-01-16 11:21	2021-01-16 11:51	232100030010 – 232100200010	32.4
2021-01-16 22:03	2021-01-16 22:33	232100230010 – 232100230010	1.8
2021-01-17 01:01	2021-01-17 01:31	232100290010 – 232100300010	3.6
2021-01-22 17:44	2021-01-22 18:25	232300480010 – 232300710010	61.4
2021-01-23 13:02	2021-01-23 13:32	232300750010 – 232300800010	10.8
2021-01-23 18:22	2021-01-23 18:52	232300850010 – 232300890010	9.0
2021-01-24 00:15	2021-01-24 00:45	232300960010 – 232300960010	1.8
2021-02-14 17:03	2021-02-14 18:01	233200020010 – 233200240010	84.3
2021-02-15 17:29	2021-02-15 18:27	233200260010 – 233200300010	21.7

Table A.6. INTEGRAL upper limits (ULs).

Burst ID	ScW ID	(θ, φ) [deg.]	UL [ergcm^{-2}s^{-1}]
SRT-P-01	229500410010	156.4, -159.4	4.8×10^{-7}
SRT-P-02	229500410010	156.4, -159.4	4.2×10^{-7}
SRT-P-03	229500420010	156.0, -155.3	5.2×10^{-7}
SRT-P-04	229500420010	156.0, -155.3	4.6×10^{-7}
SRT-P-05	229500420010	156.0, -155.3	5.3×10^{-7}
SRT-P-06	229500440010	154.3, -160.2	4.9×10^{-7}
SRT-P-07	229500440010	154.3, -160.2	4.1×10^{-7}
SRT-P-08	229500440010	154.3, -160.2	5.6×10^{-7}
SRT-P-09	229500440010	154.3, -160.2	3.8×10^{-7}
SRT-P-10	230700380010	117.1, 147.8	4.3×10^{-7}
SRT-P-11	232600520010	118.7, -118.3	5.5×10^{-7}
SRT-P-12	232600530010	118.7, -118.3	4.8×10^{-7}
SRT-P-13	232600530010	118.7, -118.3	3.7×10^{-7}
SRT-P-14	233100630010	50.7, -70.8	1.3×10^{-7}
uGMRT-01	240000130010	75.6, 93.6	2×10^{-7}
uGMRT-02	240000130010	75.6, 93.6	1.1×10^{-7}
uGMRT-03	240000140010	73.4, 94.2	1.8×10^{-7}
uGMRT-04	240000140010	73.4, 94.2	1.5×10^{-7}
uGMRT-05	240000140010	73.4, 94.2	1.4×10^{-7}
uGMRT-06	240000150021	73.1, 95.0	2.4×10^{-7}
uGMRT-07	240000150021	73.1, 95.0	1.5×10^{-7}

Notes. The second column is the ID of the Science Window Data catalogue, the third column contains the off-axis angles the fourth column contains the ULs for each burst, as discussed in Sect. 2.3.3.

Table A.7. *Swift* coverage and flux upper limits (ULs, 0.3–10 keV band).

Start time (topocentric)	Stop time (topocentric)	UL [erg cm^{-2} s^{-1}]
2020-10-22 05:33:59	2020-10-27 18:09:56	3.0×10^{-13}
2020-11-08 17:16:50	2020-11-12 15:31:56	2.7×10^{-13}
2020-12-09 04:06:58	2020-12-15 11:34:56	3.7×10^{-13}
2020-12-30 18:17:55	2021-01-01 11:49:56	4.3×10^{-13}
2021-01-10 02:40:33	2021-01-16 02:25:56	2.6×10^{-13}
2021-01-29 16:25:31	2021-02-02 16:25:55	3.1×10^{-13}
2021-03-02 13:27:42	2021-03-06 14:34:56	3.0×10^{-13}
2021-03-17 13:16:26	2021-03-23 15:57:56	2.6×10^{-13}
2021-04-19 12:02:25	2021-04-25 11:26:56	2.6×10^{-13}
2021-05-09 09:21:59	2021-05-14 10:40:56	3.3×10^{-13}
2021-05-24 09:11:17	2021-05-25 10:49:56	6.8×10^{-13}
2021-06-07 08:07:52	2021-06-13 07:48:56	2.7×10^{-13}
2021-06-22 04:47:04	2021-06-28 07:17:56	2.5×10^{-13}
2021-07-08 06:05:06	2021-07-14 07:12:56	3.4×10^{-13}
2021-07-25 04:47:26	2021-07-31 10:47:56	3.0×10^{-13}

Table A.8. *Insight*–HXMT high-energy upper limits (ULs) for the 6 observed FRBs .

Burst ID	Spectral model[a]	Time interval[b] [s]	Bin time [ms]	Fluence UL (1-30 keV) [10^{-10} erg cm^{-2}]	Confidence level (Gaussian 2σ)
SRT-P-01	PL $\Gamma = 2$	[−16, +100]	1	1.6	2.8
SRT-P-01	PL $\Gamma = 2$	[−16, +100]	16	2.7	2.5
SRT-P-01	PL $\Gamma = 2$	[−16, +100]	128	6.6	3.0
SRT-P-01	OTTB $kT = 50$ keV	[−16, +100]	1	2.2	2.8
SRT-P-01	OTTB $kT = 50$ keV	[−16, +100]	16	3.9	2.5
SRT-P-01	OTTB $kT = 50$ keV	[−16, +100]	128	9.5	3.0
SRT-P-01	OTTB $kT = 200$ keV	[−16, +100]	1	2.3	2.8
SRT-P-01	OTTB $kT = 200$ keV	[−16, +100]	16	4.1	2.5
SRT-P-01	OTTB $kT = 200$ keV	[−16, +100]	128	9.9	3.0
SRT-P-02	PL $\Gamma = 2$	[−100, +100]	1	2.0	3.0
SRT-P-02	PL $\Gamma = 2$	[−100, +100]	16	3.5	3.6
SRT-P-02	PL $\Gamma = 2$	[−100, +100]	128	7.8	2.9
SRT-P-02	OTTB $kT = 50$ keV	[−100, +100]	1	2.8	3.0
SRT-P-02	OTTB $kT = 50$ keV	[−100, +100]	16	5.0	3.6
SRT-P-02	OTTB $kT = 50$ keV	[−100, +100]	128	11	2.9
SRT-P-02	OTTB $kT = 200$ keV	[−100, +100]	1	2.9	3.0
SRT-P-02	OTTB $kT = 200$ keV	[−100, +100]	16	5.2	3.6
SRT-P-02	OTTB $kT = 200$ keV	[−100, +100]	128	12	2.9
SRT-P-07	PL $\Gamma = 2$	[−36, +100]	1	1.6	3.2
SRT-P-07	PL $\Gamma = 2$	[−36, +100]	16	2.7	3.3
SRT-P-07	PL $\Gamma = 2$	[−36, +100]	128	5.5	3.0
SRT-P-07	OTTB $kT = 50$ keV	[−36, +100]	1	2.2	3.2
SRT-P-07	OTTB $kT = 50$ keV	[−36, +100]	16	3.9	3.3
SRT-P-07	OTTB $kT = 50$ keV	[−36, +100]	128	7.8	3.0
SRT-P-07	OTTB $kT = 200$ keV	[−36, +100]	1	2.3	3.2
SRT-P-07	OTTB $kT = 200$ keV	[−36, +100]	16	4.1	3.3
SRT-P-07	OTTB $kT = 200$ keV	[−36, +100]	128	8.2	3.0
SRT-P-08	PL $\Gamma = 2$	[−51, +100]	1	1.6	3.1
SRT-P-08	PL $\Gamma = 2$	[−51, +100]	16	2.7	3.2
SRT-P-08	PL $\Gamma = 2$	[−51, +100]	128	5.5	2.9
SRT-P-08	OTTB $kT = 50$ keV	[−51, +100]	1	2.2	3.1
SRT-P-08	OTTB $kT = 50$ keV	[−51, +100]	16	3.9	3.2
SRT-P-08	OTTB $kT = 50$ keV	[−51, +100]	128	7.8	2.9
SRT-P-08	OTTB $kT = 200$ keV	[−51, +100]	1	2.3	3.1
SRT-P-08	OTTB $kT = 200$ keV	[−51, +100]	16	4.1	3.2

Table A.8. continued.

Burst ID	Spectral model[a]	Time interval[b] [s]	Bin time [ms]	Fluence UL (1-30 keV) [10^{-10} erg cm^{-2}]	Confidence level (Gaussian 2σ)
SRT-P-08	OTTB kT = 200 keV	[−51, +100]	128	8.2	2.9
SRT-P-09	PL Γ = 2	[−100, +100]	1	1.6	2.5
SRT-P-09	PL Γ = 2	[−100, +100]	16	3.1	3.0
SRT-P-09	PL Γ = 2	[−100, +100]	128	7.0	2.9
SRT-P-09	OTTB kT = 50 keV	[−100, +100]	1	2.2	2.5
SRT-P-09	OTTB kT = 50 keV	[−100, +100]	16	4.5	3.0
SRT-P-09	OTTB kT = 50 keV	[−100, +100]	128	10	2.9
SRT-P-09	OTTB kT = 200 keV	[−100, +100]	1	2.3	2.5
SRT-P-09	OTTB kT = 200 keV	[−100, +100]	16	4.6	3.0
SRT-P-09	OTTB kT = 200 keV	[−100, +100]	128	11	2.9
uGMRT-01	PL Γ = 2	[−100, +100]	1	1.6(3.6)[c]	2.7
uGMRT-01	PL Γ = 2	[−100, +100]	16	3.1(8.7)[c]	3.4
uGMRT-01	PL Γ = 2	[−100, +100]	128	6.6(30)[c]	3.3
uGMRT-01	OTTB kT = 50 keV	[−100, +100]	1	2.2(6.8)[c]	2.7
uGMRT-01	OTTB kT = 50 keV	[−100, +100]	16	4.5(16)[c]	3.4
uGMRT-01	OTTB kT = 50 keV	[−100, +100]	128	9.5(56)[c]	3.3
uGMRT-01	OTTB kT = 200 keV	[−100, +100]	1	2.3(12)[c]	2.7
uGMRT-01	OTTB kT = 200 keV	[−100, +100]	16	4.6(29)[c]	3.4
uGMRT-01	OTTB kT = 200 keV	[−100, +100]	128	11(97)[c]	3.3
uGMRT-02	PL Γ = 2	[−100, +27.7]	1	2.4[d]	2.6
uGMRT-02	PL Γ = 2	[−100, +27.7]	16	4.7[d]	3.1
uGMRT-02	PL Γ = 2	[−100, +27.7]	128	11.[d]	2.9
uGMRT-02	OTTB kT = 50 keV	[−100, +27.7]	1	2.6[d]	2.6
uGMRT-02	OTTB kT = 50 keV	[−100, +27.7]	16	5.1[d]	3.1
uGMRT-02	OTTB kT = 50 keV	[−100, +27.7]	128	12.[d]	2.9
uGMRT-02	OTTB kT = 200 keV	[−100, +27.7]	1	2.6[d]	2.6
uGMRT-02	OTTB kT = 200 keV	[−100, +27.7]	16	5.3[d]	3.1
uGMRT-02	OTTB kT = 200 keV	[−100, +27.7]	128	12[d]	2.9

Notes. [a]PL: power-law with photon index Γ = 2; OTTB: optically thin thermal bremsstrahlung. [b]TDB since FRB time calculated at infinite frequency. [c]Values among parentheses refer to the 1–100 keV passband. [d]Values refer to the 10–30 keV passband.